Journal of Medicinal Chemistry

Article

Rational Design of Suprastat, a Novel Selective Histone Deacetylase 6 Inhibitor with the Ability to Potentiate Immunotherapy in Melanoma Models

Satish Noonepalle, Sida Shen, Jakub Ptacek, Maurício T Tavares, GuiPing Zhang, Jan Stransky, Jiri Pavlicek, Glaucio M Ferreira, Melissa Hadley, Guido Pelaez, Cyril Ba#inka, Alan P. Kozikowski, and Alejandro Villagra

J. Med. Chem., **Just Accepted Manuscript** • DOI: 10.1021/acs.jmedchem.0c00567 • Publication Date (Web): 20 Aug 2020

Just Accepted

is published by the American Chemical Society. 1155 Sixteenth Street N.W., Washington, DC 20036

Rational Design of Suprastat, a Novel Selective Histone Deacetylase 6 Inhibitor with the Ability to Potentiate Immunotherapy in Melanoma Models

Satish Noonepalle[a,†], Sida Shen[b,†,‡], Jakub Ptáček[d], Maurício T. Tavares[b,], Guiping Zhang[b], Jan Stransky[e], Jiri Pavlicek[e], Glaucio M. Ferreira[f], Melissa Hadley[a], Guido Pelaez[a], Cyril Bařinka[,d], Alan P. Kozikowski*[,c], Alejandro Villagra*[,a]*

[a] Department of Biochemistry and Molecular Medicine, The George Washington University, Washington, District of Columbia 20052, United States

[b] Department of Medicinal Chemistry and Pharmacognosy, College of Pharmacy, University of Illinois at Chicago, Chicago, Illinois 60612, United States

[c] Bright Minds Biosciences, Toronto, ON M5H 3V9, Canada

[d] Laboratory of Structural Biology, Institute of Biotechnology of the Czech Academy of Sciences, BIOCEV, Prumyslova 595, 252 50 Vestec, Czech Republic

[e] Centre of Molecular Structure, Institute of Biotechnology of the Czech Academy of Sciences, BIOCEV, Prumyslova 595, 252 50 Vestec, Czech Republic

[f] Department of Pharmacy, School of Pharmaceutical Sciences, University of São Paulo, São Paulo, SP, 05508-000, Brazil

[†] These authors contributed equally to this work.

KEYWORDS: catalytic domain 2, hydrogen-bonding interaction, acetylated α-tubulin, immunoregulation, combination therapy

ABSTRACT

Selective inhibition of histone deacetylase 6 (HDAC6) is being recognized as a therapeutic approach for cancers. In this study, we designed a new HDAC6 inhibitor, named Suprastat, using *in silico* simulations. X-ray crystallography and molecular dynamics simulations provide strong evidence to support the notion that the aminomethyl and hydroxyl groups in the capping group of Suprastat establish significant hydrogen bond interactions, either direct or water-mediated, with residues D460, N530, and S531, which play a vital role in regulating the deacetylase function of the enzyme and which are absent in other isoforms. *In vitro* characterization of Suprastat demonstrates subnanomolar HDAC6 inhibitory potency and a hundred- to a thousand-fold HDAC6 selectivity over the other HDAC isoforms. *In vivo* studies reveal that a combination of Suprastat and anti-PD1 immunotherapy enhances anti-tumor immune response, mediated by a decrease of pro-tumoral M2 macrophages and increased infiltration of anti-tumor CD8+ effector and memory T-cells.

INTRODUCTION

Reversible acetylation of lysine side chains on the surface of enzymes and other proteins is modulated by histone acetyltransferases (HATs) and histone deacetylases (HDACs). Protein lysine acetylation or deacetylation serves as a key regulatory pathway for various cellular processes, such as transcription, cell cycle, and cellular metabolism.[1-3] HDACs have been demonstrated to be effective targets for the treatment of cancer, neurological diseases, and immune disorders.[4-6] Up to date, 11 zinc ion (Zn^{2+})-dependent HDACs (Class I, II, and IV) and seven nicotinamide adenine dinucleotide (NAD^{+})-dependent sirtuins (SIRTs) (Class III) have been identified. Unlike other members, HDAC6 in Class IIb is unique due to its ability to deacetylate a number of non-histone proteins as its preferred substrates, such as α-tubulin and HSP-90.[7, 8] HDAC6 inhibitors (HDAC6is), Ricolinostat (ACY-1215), Citarinostat (ACY-241), and KA2507 are being evaluated in clinical trials for various types of cancers through either monotherapy or a combination approach,[9] although they are only partially selective HDAC6is. Therefore, HDAC6is have emerged as a promising approach for cancer therapy.

Immunomodulatory properties of HDAC6is have deemed them as therapeutic agents for cancer immunotherapy. It has been reported that HDAC6 interacts with the transcription factor STAT3, which is a primary regulator of immune responses in the tumor microenvironment,[10] and that it regulates STAT3-mediated gene expression.[11] In antigen-presenting cells (APCs), such as macrophages and dendritic cells, selective inhibition of HDAC6 leads to a decreased production of immunosuppressive cytokine

IL-10, thereby retaining the proinflammatory state of APCs.[11] In melanoma tumor cells, HDAC6 inhibition leads to a decreased level of the immunosuppressive molecule PD-L1 by affecting the recruitment and activation of STAT3.[12] Furthermore, using the syngeneic murine melanoma mouse model, we recently demonstrated that a combination therapy comprised of selective HDAC6is and PD-1 antibody leads to significantly improved effects on tumor growth compared to a single therapy,[13] thereby underscoring the immunomodulatory capability of selective HDAC6is.

The structure of one HDAC6i typically contain: a) a zinc-binding group (ZBG) establishing essential coordination with the Zn^{2+} ion in the active site; b) a linker region filling the hydrophobic space between the catalytic site and the outer surface; c) a capping group (cap) interacting with residues on the surface. The phenylhydroxamate-based HDAC6is feature the critical ZBG and linker for selective and potent HDAC6 inhibition that originated from the invention of Tubastatin A (TubA, Figure 1A).[9, 14-18] HDAC6is are largely comprised of arylhydroxamate-based analogs.[9] However, the recent development of oxadiazole-based selective HDAC6is by pharmaceutical companies[9] may provide a new opportunity to refine the druglike properties (e.g., metabolic stability, permeability, and mutagenicity)[19-21] of HDAC6is. Crystallographic studies of several ligands complexed with *Danio rerio* HDAC6 (zHDAC6) have revealed that most selective HDAC6is containing phenylhydroxamate exhibit an unusual monodentate Zn^{2+} coordination geometry.[22, 23] On the other hand, a typical canonical bidentate Zn^{2+} coordination was observed in a number of zHDAC6 crystals complexing with HDACis bearing alkylhydroxamate or capless arylhydroxamate.[24-26]

In addition, the phenylhydroxamate moiety is sandwiched by F583 and F643 in the hydrophobic tunnel, establishing a double π-stacking interaction.

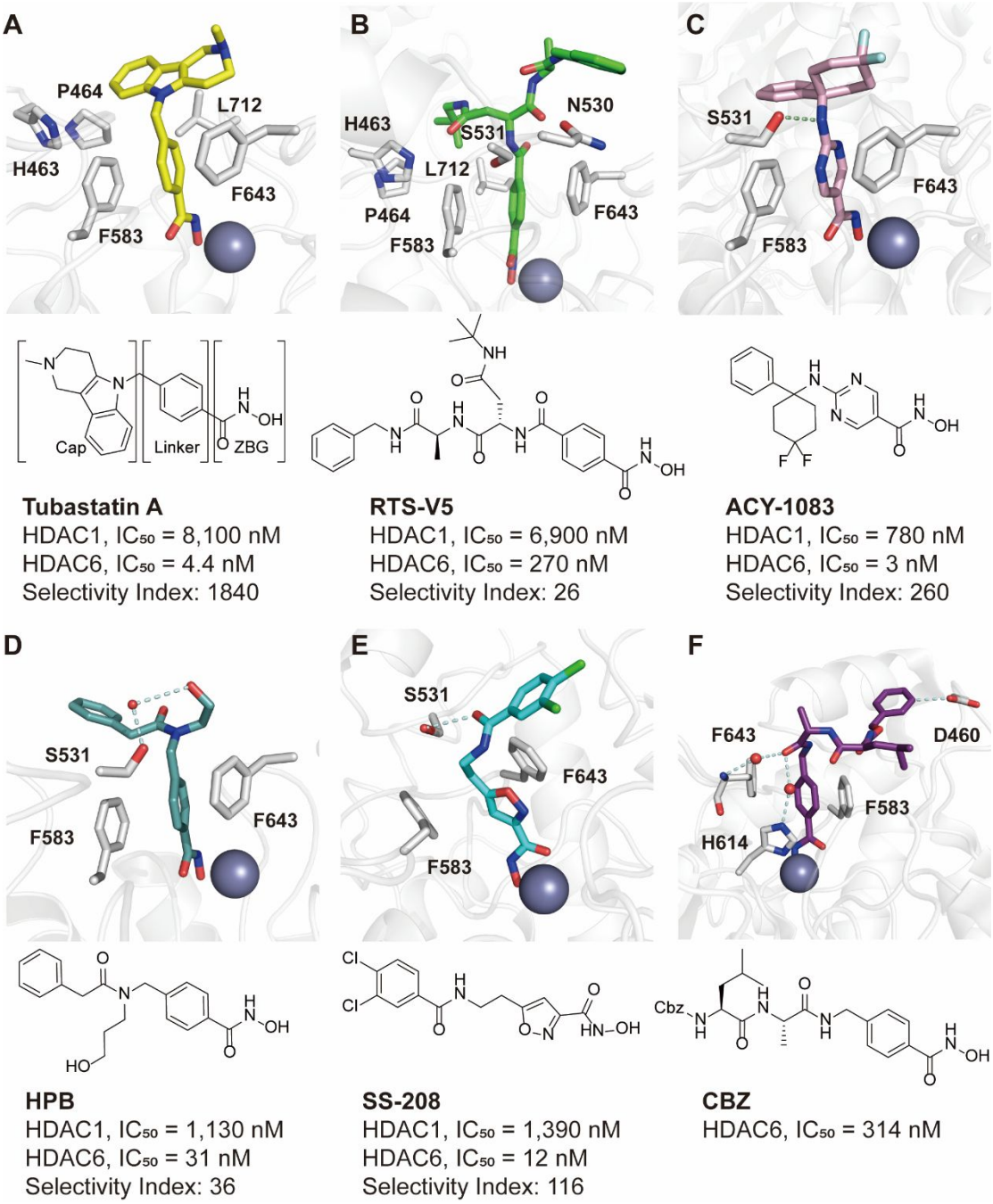

Figure 1. Crystal structures of zHDAC6 complexes with selective HDAC6is (**A**) Tubastain A (yellow, PDB code 6THV) (**B**) RTS-V5 (green, PDB code 6CW8) (**C**) ACY-1083 (pink, PDB code 5WGM) (**D**) HPB (blue, PDB code 5WGK) (**E**) SS-208 (cyan, PDB code 6R0K) (**F**) CBZ (purple, PDB code 6PZU). Selective amino acid

residues in HDAC6 are indicated in stick representation with carbon atoms in grey, oxygen atoms in red, nitrogen atoms in blue colors, whereas active-site zinc ion and water molecules are indicated as silver and red spheres, respectively. IC_{50} values for HDAC1 and HDAC6, along with selectivity indices, are indicated for each HDAC6 inhibitor.

Among zinc-dependent HDACs, only HDAC6 contains a large open basin approximately 14 Å wide. Thus, a lot of selective HDAC6is consist of a bulky and rigid cap to occupy the broad rim of the pocket.[22] Polycyclic aromatic rings are often considered as useful caps in selective HDAC6is that can form robust hydrophobic engagements with the L1 loop pocket defined by key residues H463, P464, F583, and L712, which is considered as the selectivity-determining area.[25-27] The crystal structure of the enzyme in complex with TubA (PDB code 6THV) is shown in Figure 1A as an example.[28] Recent findings provide additional examples, such as Resminostat (PDB code 6PZR), whose cap engages with another pocket defined by the L2 loop.[29] Moreover, the bifurcated cap of the dual HDAC-proteasome inhibitor RTS-V5 can occupy both L1 and L2 pockets and interact with the nearby residues G640-N645 (Figure 1B, PDB code 6CW8).[30, 31]

Besides hydrophobic and π-stacking interactions, HDAC6 crystals in complex with selective HDAC6is also indicate that capping or linker groups form additional hydrogen bonds with the residue S531 inside the pocket: a) The NH group on the linker of pyrimidinylhydroxamate-based ACY-1083 shows a direct hydrogen-bonding

interaction to the hydroxyl group of S531 (Figure 1C, PDB code 5WGM).[23] b) The hydroxyl group on the *n*-propyl tail chain of HPB forms a water-mediated hydrogen bond with S531 (Figure 1D, PDB code 5WGK).[23] c) The carbonyl group on the amide connecting unit of isoxazole-3-hydroxamate-based SS-208 interacts with S531 at a distance of 3.3 Å (Figure 1E PDB code 6R0K).[26] Moreover, hydrogen-bonding interactions with other residues (e.g., D460 and F643) are also observed in zHDAC6 crystal complexes: a) Ricolinostat establishes water-mediated hydrogen-bonding interactions with D460 and S531 through its aminopyrimidinyl core and amide linkage, respectively (PDB code 5WGL).[23] b) zHDAC6 in the complex with a Cbz-protected dipeptide (Leu-Ala) capped HDAC6i CBZ (Figure 1F, PDB code 6PZU) reveals that the phenyl ring of the Cbz protecting group forms a carbon-hydrogen bond with D460. In contrast, hydrogen-bond interactions mediated by water molecules are observed with the imidazole ring of H614 and the amino group of F643.[29] Noteworthy, S531 is critical for substrate recognition and engages with the NH group of the *N*-acetyllysine moiety through a hydrogen-bond interaction.[24] It was also found that a single mutation (S531A) in sequence encoding zHDAC6-CD2 decreased the catalytic efficiency by 258-fold.[24] Moreover, It was reported by the Matthias group that double mutations (W459A and D460A) and other single mutations (N530A, N530D, or S531A) significantly reduced α-tubulin deacetylation.[22] It should be noted that N530 of zHDAC6 corresponds to D567 in the human ortholog. Surprisingly, the N530D substitution in zHDAC6 led to a substantial decrease in the deacetylation efficacy of α-tubulin. At the same time, it has been reported by the Christianson group that the N530A substitution in zHDAC6

and D567A substitution in hHDAC6 did not significantly influence HDAC6 deacetylase activity using a fluorogenic substrate derived from histone H4[24] Apparently, the residue might play an important role in the interaction interface with proteinaceous substrates (e.g., tubulin), but not small peptides. The detailed understanding of the N530 (D567) role in substrate recognition warrants further studies.

Overall, we hypothesized that establishing specific hydrogen-bonding interactions with these key residues, which play crucial roles in regulating the deacetylation function of HDAC6 and which are absent in other isoforms, might lead to enhanced potency and excellent HDAC6 isoform selectivity.[32] Currently, a typical strategy in the discovery of selective HDAC6is relies on modifications of aromatic capping groups to strengthen hydrophobic interactions with residues of the L1-loop pocket.[9, 16, 17] As an alternative approach, we designed new analogs based on the Nexturastat A (NextA) scaffold by incorporating polar groups to interact with key residues of the HDAC6 pocket. Integrated structural and biological characterization demonstrates that one analog, named Suprastat, represents a new generation of selective HDAC6i.

RESULTS AND DISCUSSION

Design and synthesis of Suprastat (6a). NextA (Figure 2A, left) comprises a classical phenylhydroxamate zinc-binding core linked to a urea-based cap featuring a phenyl ring and an *n*-butyl side chain, which exhibits good affinity and selectivity for HDAC6.[33] The HDAC6/NextA crystal (PDB code 5G0I, Figure 2B) reveals that there is no direct enzyme-inhibitor hydrogen bonding interaction between the cap and the

pocket. Instead, the steric complementarity between the bulky cap and the 3D contour of the pocket drives important hydrophobic interactions. NextA exhibited minimal antiproliferative activity against a variety of human cancer cell lines and induced G1 cell-cycle arrest without eliciting apoptosis.[26, 34] Moreover, it was found that NextA down-regulated the level of the immunosuppressive molecule PD-L1 (*CD274*) in melanoma cells and additionally impaired melanoma tumor growth in immunocompetent mice mediated by increased tumor-specific immunogenic signals.[13] Recent findings further demonstrated that a combination treatment employing NextA along with anti-PD1 immune blockade resulted in enhanced T-cell infiltration coupled with a decrease of pro-tumor M2 macrophages in the tumor microenvironment, leading to significant tumor growth inhibition and a higher survival rate compared to monotherapy.[13] Given the well-understood molecular basis for its selective inhibition of HDAC6 as well as its efficacy in established murine melanoma models, we selected NextA as a parent scaffold for designing the next generation of HDAC6is.

We reasoned that the derivatization of the NextA cap with polar groups could further increase potency and selectivity *via* potential interactions with the residues at the rim region of the HDAC6 catalytic core. Molecular docking studies using the HDAC6/NextA complex as a template were performed for a series of newly designed NextA derivatives. We examined their capacity to extend the interaction interface of the inhibitor cap with the HDAC6 rim residues. The most promising derivative, named Suprastat, contains an aminomethyl group at the para position of the phenyl ring and a hydroxyl group at the end of the *n*-butyl chain attached to the proximal urea nitrogen

(Figure 2A, right). Based on the *in silico* predictions, the positively charged aminomethyl and hydroxybutyl branches of Suprastat interact with the carboxyl group of D460 and the main chain amino group of F643, respectively (Figure 2B).

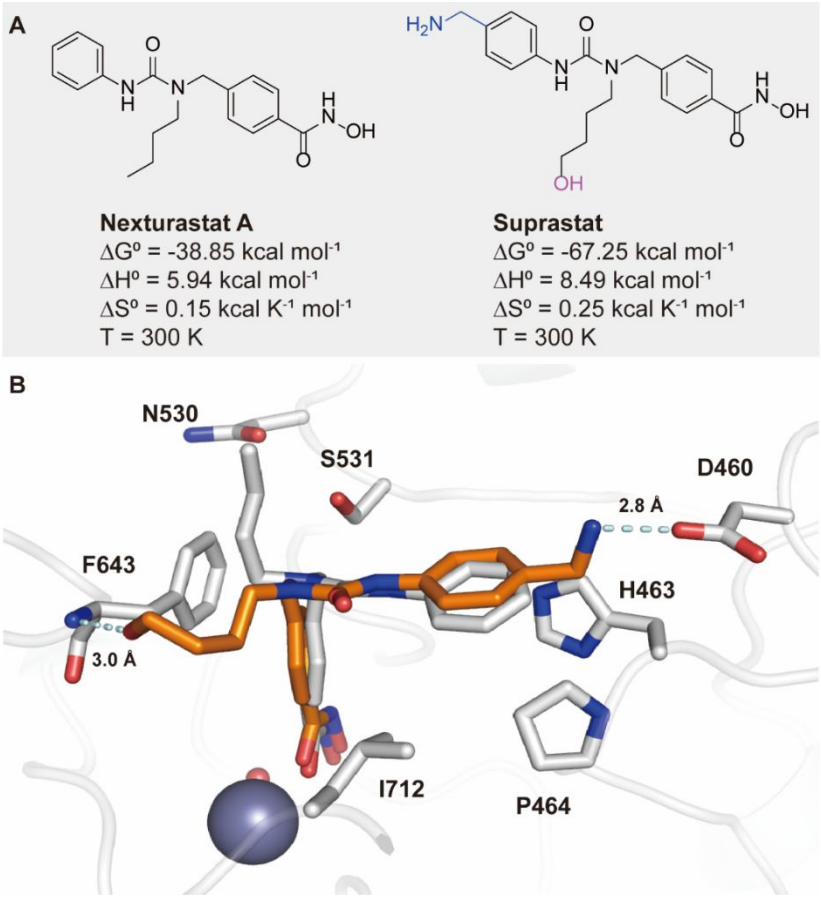

Figure 2. *In silico* design of Suprastat by NextA derivatization. (**A**) Structures of phenylhydroxamate-based Nexturastat A (left) and Suprastat (right). (**B**) Molecular docking of Suprastat (orange) based on the HDAC6/Nexturastat A complex (PDB code 5G0I; silver) with an indication of the additional interactions created by the aminomethyl and hydroxybutyl polar groups with residues D460 and F643 at the rim of the catalytic pocket of HDAC6.

Moreover, we performed relative binding free energy calculations[35] on the

HDAC6/NextA and HDAC6/Suprastat complexes, respectively. The results indicate that the HDAC6/Suprastat complex shows a much lower free energy of binding (ΔG^0 = -67.25 kcal mol^{-1}) compared to HDAC6/NextA (ΔG^0 = -38.85 kcal mol^{-1}), suggesting an improved affinity of Suprastat for the HDAC6 catalytic pocket. The enthalpic (ΔH^0) and entropic (ΔS^0) contributes to both ΔG^0 values, determined by the Gibbs free energy equation (Figure 2A). The results suggest that the improved affinity of Suprastat is accompanied by a more substantial entropic gain ($-T\Delta S^0$).

Scheme 1. Synthetic route to **6a-b** and **6d-f**[a]

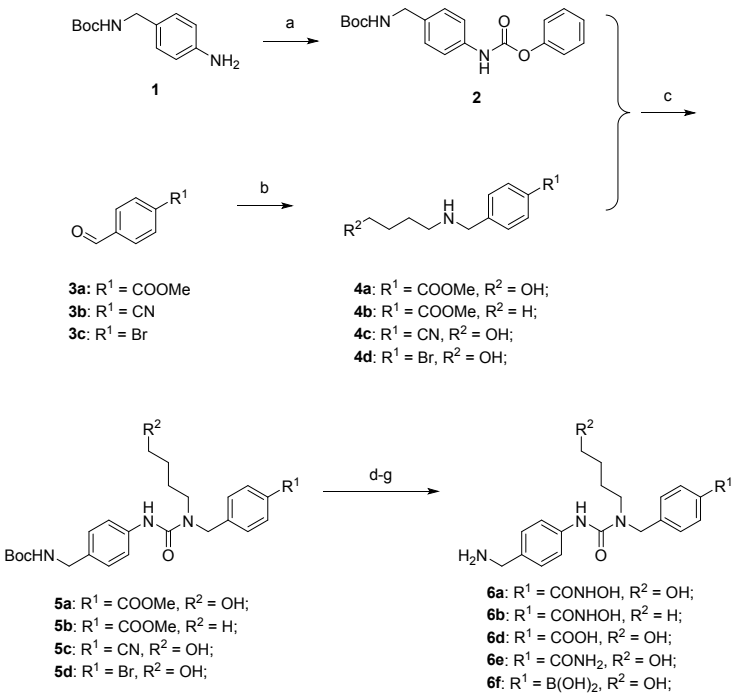

[a]Reagents and conditions. (a) phenyl chloroformate, K_2CO_3, acetone, rt, 2 h; (b) i) 4-amino-1-butanol for **4a**, **4c**, and **4d** and *n*-butylamine for **4b**, EtOH, reflux, 2 h; ii) $NaBH_4$, MeOH, 0°C-rt, 2 h; (c) **2**, TEA, THF, reflux, 2 h; (d) for **6a** and **6b**: i) aq. NH_2OH (50%), NaOH, THF/MeOH, 0°C, 15 min; ii) TFA, THF, rt, 0.5 h; (e) for **6d**: i) 1N NaOH, THF/MeOH, rt, overnight; ii) TFA, THF, rt, 0.5 h; (f) for **6e**: i) H_2O_2

(30%), K_2CO_3, DMSO, rt, 5 h; ii) TFA, THF, rt, 0.5 h; (g) for **6f**: i) B_2pin_2, KOAc, Pd(dppf)Cl_2, DMF, 80°C, overnight; ii) $NaIO_4$, NH_4OAc, acetone-H_2O, rt, overnight; iii) TFA, THF, rt, 0.5 h.

The synthetic route to Suprastat was initiated by the preparation of a carbamate intermediate **2** from phenyl chloroformate and aniline **1** under K_2CO_3/acetone conditions. On the other hand, methyl 4-formylbenzoate **3a** underwent a rapid reductive amination with 4-amino-1-butanol to provide intermediate **4a**. Subsequently, the combination reaction between **2** and **4a** under TEA/THF conditions afforded the key urea precursor **5a,** which was further converted to the final hydroxamate product **6a** (Suprastat) using aqueous hydroxylamine under basic conditions followed by TFA/THF to remove the Boc group. For evaluation together with Suprastat in the following biological experiments, analog **6b** bearing an aminomethyl group and the original *n*-butyl chain attached to the proximal urea nitrogen was also prepared from **3a** and *n*-butylamine using the same synthetic route to Suprastat. The synthesis of **6c** (Table 1), which contains a hydroxylbutyl side chain but no aromatic substituent, has been reported in our prior work.[36] Moreover, non-hydroxamate analogs **6d-f** containing the same cap with Supratstat were prepared and evaluated to explore if additional hydrogen binding interactions would be able to retain activity without a hydroxamate ZBG, inspired by ketone/amide-based Class I HDACis.[37-39] The carboxylic acid analog **6d** was directly afforded from the urea ester **5a** through hydrolysis under basic condition and Boc deprotection. To synthesize the amide analog **6e**, 4-

formylbenzonitrile **3b** underwent the two-step reductive amination followed by the reaction with carbamate **2** to generate the intermediate urea **5c**. The nitrile group in **5c** was further converted to an amide group by treating with aqueous hydrogen peroxide solution under basic condition, and the final product **6e** was afforded through Boc deprotection as described above. The synthetic route to the boronic acid analog **6f** initiated with the reductive amination of 4-bromobenzaldehyde **3c** followed by urea formation using the same procedures as above to give the intermediate urea **5d**. The precursor **5d** underwent coupling reaction with bis(pinacolato)diboron under KOAc/Pd(dppf)Cl_2 conditions. In the end, the desired boronic acid product **6f** was obtained through pinacol deprotection and Boc deprotection under $NaIO_4$/NH_4OAc and TFA/THF, respectively.

***In vitro* HDAC potency assessment**. To evaluate the influence of each additional functional group on the potency and isoform selectivity, we tested the potency of **6a-c** along with NextA against human HDACs 1-9 and 11 under optimized conditions *in vitro*.[26] It should be mentioned that our highly pure (>98%) HDAC10 preparations heterologously expressed in HEK293T cells did not show any appreciable activity using either acetylspermidine[40] or RHKK(Ac)AMC (typically used by Reaction Biology Corp, Malvern, PA) as the substrate for HDAC10 profiling. Therefore, the IC_{50} values of HDAC10 were not included. Results in Table 1 suggest that **6a** and **6c** are more potent and selective HDAC6is (IC_{50} = 0.4 vs. 0.5 nM) with at least 290-fold selectivity over Class I isoforms HDAC1-3 and 8 and a thousand-fold selectivity over

Class IIa isoforms HDAC4, 5, 7, and 9. Moreover, **6a-c** did not show activity against the Class IV isoform HDAC11 up to 50 μM. It shall be noted that experimental IC_{50} values in the range of 0.2–0.4 nM for HDAC6 are at the limit of our assay that uses approximately 0.6 nM concentration of the full-length enzyme (as determined by absorbance measurements at 280 nm). IC_{50} values for Suprastat and **6c** are thus at the limit of our assay, and these two inhibitors can theoretically have an even higher potency than reported here. Overall, the inhibition data suggest that the hydroxylbutyl chain contributes more prominently towards the increase in HDAC6 affinity and selectivity compared to the aminomethyl group. Additionally, the incorporation of the polar aminomethyl and hydroxylbutyl groups into the inhibitors **6a-c** increases the number of heavy atoms but decreases their clogP (calculated by SwissADME[41]) relative to NextA (Table 2), which leads to significantly elevated lipophilic ligand efficiencies (LipE),[42] especially **6a** ((LipE = 7.57 (**6a**) vs. 6.19 (NextA)), although the ligand efficiencies (LE) of **6a** and **6b** are slightly lower.[43] Taken together, compared to NextA and related analogs, Suprastat (**6a**) bearing both hydroxybutyl and aminomethyl moieties showed improved potency against HDAC6 and excellent selectivity over the other HDAC isoforms. At the same time, it also exhibits the highest LipE value due to its significantly decreased clogP. On the other hand, the inhibitory potency of the non-hydroxamate-based analogs **6d-f** comprised of carboxylic acid, amide, or boronic acid as alterative ZBGs against HDAC6 was severely compromised (Supplementary Table S1), which would indicate that the additional hydrogen bonding interactions between the cap and HDAC6 pocket are not strong enough to maintain nanomolar potency when

the critical hydroxamate-Zn^{2+} coordination is absent.

Table 1. *In vitro* HDAC profiles of **6a-c** and NextA [a]

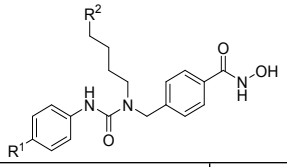

Compound	Suprastat (6a)		6b		6c [b]		NextA	
R^1	CH_2NH_2		CH_2NH_2		H		H	
R^2	OH		H		OH		H	
Isoform	IC_{50}, nM	SI [c]	IC_{50}, nM	SI	IC_{50}, nM	SI	IC_{50}, nM	SI
HDAC6	0.4 ± 0.0	1	0.9 ± 0.7	1	0.5 ± 0.4	1	1.6 ± 0.4	1
HDAC1	117 ± 10	293	80 ± 45	89	148 ± 9	296	151 ± 20	94
HDAC2	176 ± 21	440	281 ± 28	312	268 ± 16	536	276 ± 96	173
HDAC3	352 ± 2	880	443 ± 108	492	581 ± 18	1,160	1,420 ± 145	887
HDAC4	8,250 ± 1,350	20,600	23,100 ± 226	25,700	14,000 ± 1,380	27,900	14,800 ± 1,700	9,250
HDAC5	3,420 ± 373	8,550	10,100 ± 162	11,200	9,130 ± 119	18,300	6,620 ± 2,660	4,140
HDAC7	1,470 ± 56	3,680	9,000 ± 1,110	10,000	1,930 ± 70	3,870	2,430 ± 300	1,520
HDAC8	498 ± 58	1,250	614 ± 58	682	478 ± 97	956	988 ± 264	618
HDAC9	6,270 ± 177	15,700	17,300 ± 4,990	19,200	29,700 ± 4,190	59,50	2,000 ± 770	1,250
HDAC11	>50,000	-	>50,000	-	>50,000	-	10,600 ± 2,200	6,630

[a] IC_{50} values are the mean of two experiments ± SEM calculated by non-linear regression analysis from experimental v_i/v_0 values for each HDAC isoform. [b] **6c** was originally published as compound **7b** in Ref 36. [c] SI: HDAC6 selectivity index over other HDAC isoforms.

***In vitro* ADME profiling of 6a-c**. As a part of the initial ADME profiling, we determined the stability of studied compounds in PBS, simulated gastric fluid (SGF), human plasma, and rat liver microsomes, as well as protein binding in human plasma (Table 2). Overall, the stability of Suprastat (**6a**) is excellent, ranging from >24 h in PBS to a half-life ($t_{1/2}$) of 173 min in rat liver microsomes. In line with predicted physicochemical characteristics, plasma binding of Suprastat is much lower (2% of

plasma protein-bound fraction), which is beneficial for elevating free drug concentration *in vivo*, compared to the more hydrophobic parent compound NextA (89%). In comparison, plasma-bound fractions of singly modified analogs **6b** and **6c** both are approximately 50%.

Table 2. Ligand efficiency and *in vitro* ADME profiling of **6a-c** and NextA

Compound	Suprastat (6a)	6b	6c	NextA
clog $P_{o/w}$ [a]	1.23	2.21	1.82	2.61
LE [b]	0.47	0.47	0.50	0.49
LipE[c]	7.57	6.59	6.98	6.19
PBS stability ($t_{1/2}$, h) [d]	>24	>24	>24	>24
SGF stability ($t_{1/2}$, h) [d]	>5	>5	>5	>5
Human plasma stability ($t_{1/2}$, h) [d]	>5	>5	>5	>5
Rat liver microsomes ($t_{1/2}$, min) [e]	177 ± 6	173 ± 71	198 ± 32	423 ± 104
Human plasma binding (%) [f]	1.9 ± 3.5	47 ± 2.0	48 ± 0.9	89 ± 0.7

[a] clog $P_{o/w}$ values were calculated by SwissADME[41] (http://www.swissadme.ch/). [b] LE: ligand efficiency = 1.4 × pIC_{50}/number of heavy atoms. [c] LipE: lipophilic ligand efficiency = pIC_{50} − clog $P_{o/w}$. [d] Data were obtained from two independent experiments run in triplicates. [e] Data are presented as the mean ± standard error from two independent experiments run in triplicates. [f] Data are presented as the mean ± standard error from two independent experiments run in duplicates.

***In vitro* characterization of 6a-c in melanoma cells**. To assess the potency and isoform selectivity of **6a-c** in cells, we performed *in vitro* analysis using the WM164 human melanoma cell line. WM164 cells are mutant for BRAF V600E, a mutation that is frequently seen in melanoma patients.[44] WM164 cells were treated with **6a-c** and NextA with a concentration range from 0.1 to 10 μM, respectively. Their abilities to

increase the levels of acetylated α-tubulin (Ac-α-tubulin) were determined by immunoblot analysis and compared side-by-side. Figures 3A-D show an increase in Ac-α-tubulin with increasing concentrations of HDAC6is but with varying magnitudes (Figure 3E). However, the increase in Ac-α-tubulin was also associated with a slight increase in the levels of acetylated histone H3 (Ac-H3), albeit at higher concentrations (Figure 3F). Treatment with Suprastat led to the highest Ac-α-tubulin levels ranging from 0.1 to 10 μM and the most significant elevation at 10 μM compared to other HDAC6is. At higher concentrations, we did observe a slight increase in the levels of Ac-H3 with Suprastat, but it was much lower than with other HDAC6is. These data thus demonstrate that Suprastat, containing both aminomethyl and hydroxylbutyl groups, exhibits better HDAC6 potency and selectivity when tested in live cells. Based on the concentration range for the α-tubulin/histone acetylation experiments, additional cytotoxicity assays were performed in SM1 murine melanoma cells. The results shown in the Supplementary Figure S1 reveal that NextA and **6b** begin to induce cytotoxicity at a concentration of 10 μM, while Suprastat and **6c** were not cytotoxic upon to 25 μM.

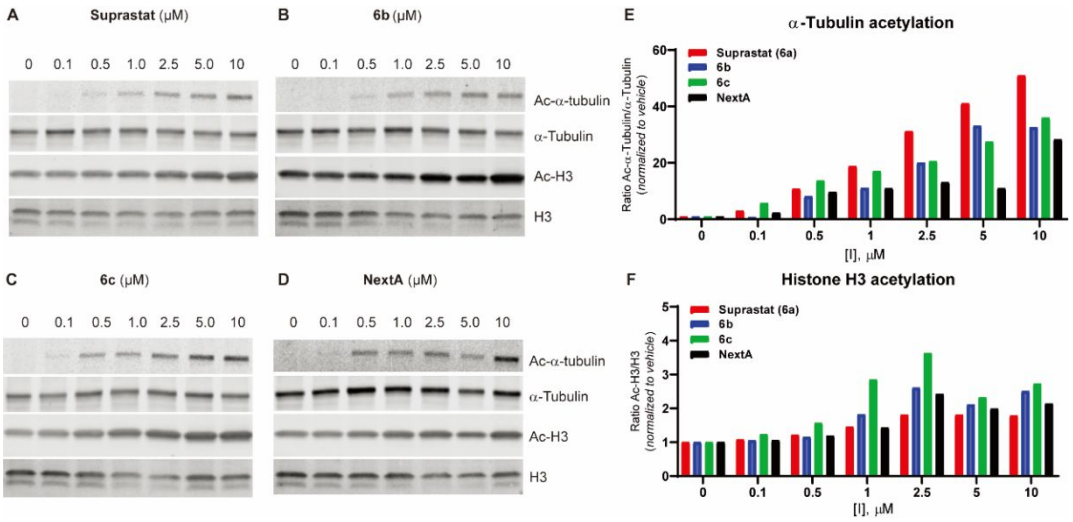

Figure 3. Suprastat is a highly selective HDAC6 inhibitor. WM164 human melanoma

cells treated overnight with increasing concentrations ranging from 0.1 μM to 10 μM for HDAC6 inhibitors Suprastat (**6a**, **A**), **6b** (**B**), **6c** (**C**), and NextA (**D**). Immunoblot analysis was performed for Ac-α-tubulin and Ac-H3. Total α-tubulin and total H3 are loading controls. (**E**) and (**F**) are densitometric analyses of the Ac-α-tubulin and Ac-H3 bands, respectively. The immunoblots were repeated at least twice to confirm accuracy, and the best representation is shown.

Functional characterization of Suprastat. Immune cells, such as macrophages, are a major cellular component of the tumor microenvironment. Tumor-associated macrophages are often tumor-promoting by secreting anti-inflammatory cytokines such as TGFβ and IL-10. We previously established that HDAC6 forms a complex with STAT3, and either pharmacological inhibition or shRNA mediated knockdown of HDAC6 decreased STAT3 recruitment at the IL10 promoter region in antigen-presenting cells.[11] In line with these experiments, as shown in Figure 4A, the treatment of mouse bone marrow-derived macrophages with 5 μM Suprastat resulted in decreased expression of *IL10* gene compared to vehicle-treated macrophages as determined by mRNA quantification. *IL10* gene expression is normalized to β-actin (*ACTB*) as the reference gene. A dose-dependent increase in the levels of Ac-α-tubulin was observed in RAW 264.7 macrophages (Supplementary Figure S2) when they were treated with increasing concentrations (1, 5, and 10 μM) of Suprastat, indicating that Suprastat affects macrophages and melanoma cells in a similar fashion. Furthermore, as shown in Figure 4B, immunoblot analysis of lysates obtained from WM164 melanoma cells

pre-treated with either Suprastat or NextA followed by exposure to IL-6 cytokine (30 ng/mL) for 20 min resulted in decreased Y705 phosphorylation of STAT3 compared to IL-6 alone. This result indicates that Suprastat, similar to NextA, mediates immunomodulatory effects by affecting HDAC6 interaction with the STAT3 transcription factor.

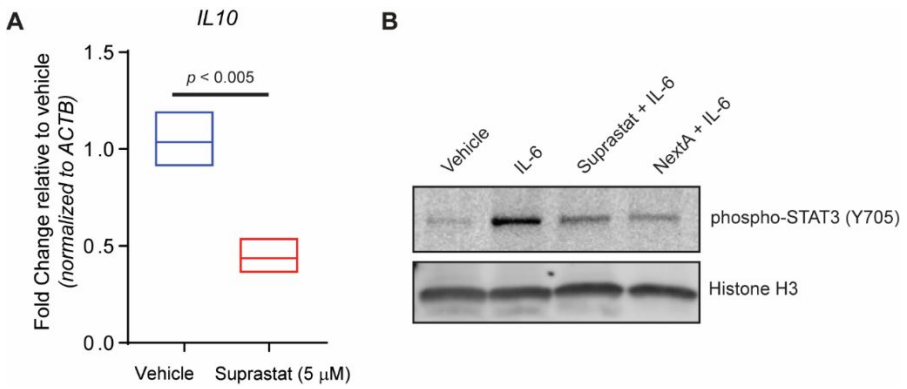

Figure 4. Suprastat modulates immune pathways through interaction with STAT3. (**A**) *IL10* gene expression was determined by quantitative PCR in bone marrow-derived macrophages exposed to interferon-gamma (20 ng/mL) and LPS (100 ng/mL). (**B**) WM164 murine melanoma cells were pre-treated with 5 μM of Suprastat or NextA followed by treatment with IL-6 (30 ng/mL) for 20 min.

***In vivo* combination study with immunotherapy**. Immunotherapy is emerging as a primary treatment modality for solid tumors; however, patients will often develop resistance, and currently, there is a need for combination therapies to increase the effectiveness of immunotherapy while overcoming resistance.[45] Using the syngeneic SM1 murine melanoma model, we previously demonstrated that pre-treatment with NextA significantly decreased tumor size in C57BL/6 mice. These mice have an active

immune system, which enables us to test immune checkpoint inhibitors such as anti-PD1 therapy. The combination of NextA and anti-PD1 treatment resulted in substantial control of tumor growth compared to single-arm therapies, suggesting that HDAC6 inhibition plays a significant role in enhancing anti-tumor immunity.[13] Following a similar approach, C57BL/6 mice harboring SM1 melanoma tumors were administered 25 mg/kg of Suprastat intraperitoneally (IP) before starting the anti-PD1 immune checkpoint blockade therapy (15 mg/kg, IP). The pre-treatment modality was performed to pre-condition the tumor microenvironment (TME) in a manner conducive to eliciting an anti-tumor immune response. As shown in Figure 5A, compared to the control (PBS) group, single-arm therapies with Suprastat similarly reduced the tumor burden as indicated by the tumor volume. However, we did not see a significant difference between Suprastat and anti-PD1 therapy. On the contrary, a combination of Suprastat and anti-PD1 therapy showed a substantial decrease in tumor burden compared to control and single therapy groups, suggesting that pre-treatment with Suprastat enhances the anti-tumor immune response resulting from the anti-PD1 therapy. Figure 5B shows the tumor growth of each mouse in the respective treatment groups. It was noted that the Suprastat and anti-PD1 therapy combined group exhibited enhanced inhibitory effects on the tumor growth before Day 14 compared to other groups. On the other hand, the combination of NextA and anti-PD1 therapy started to exhibit distinct antitumor effects after Day 20 relative to single therapy groups in our previous studies,[13] suggesting that Suprastat is capable of promoting the immunotherapy at an earlier stage.

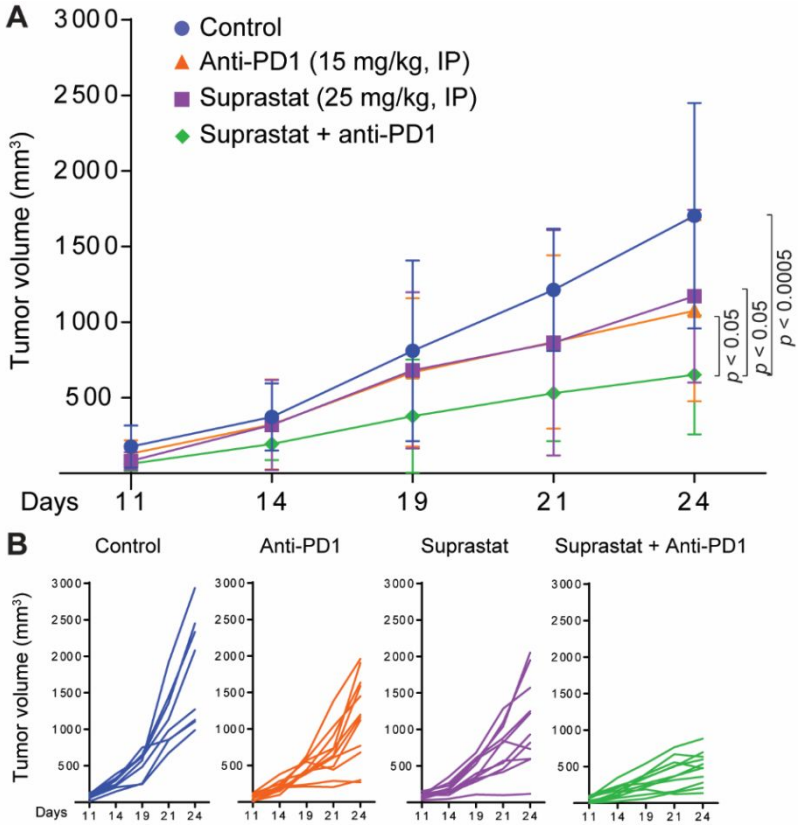

Figure 5. The combination of Suprastat with anti-PD1 immunotherapy significantly decreases tumor burden in the SM1 murine melanoma model. (**A**) Cumulative tumor growth rates in C57BL/6 mice (n = 10) after treatment with Suprastat or anti-PD1 therapy or a combination of both. Tumor growth rates of treatment groups were compared to control groups treated with PBS. (**B**) Tumor growth rates of individual mice in respective treatment groups.

Immunomodulatory properties of Suprastat. To understand the immunomodulatory properties of Suprastat, we performed a comprehensive immune cell phenotyping by flow cytometry. The number of F4/80+ CD80+ H2+ anti-tumor M1 macrophages as a percentage of CD45+ cells did not significantly change in all of the treatment groups (Figure 6A). However, Suprastat significantly decreased F4/80+ CD206+ pro-tumor

M2 macrophages (Figure 6B), thus shifting the balance towards an anti-tumor immune response as indicated by the considerably higher M1/M2 ratio (Figure 6C) in the Suprastat and combination groups relative to control and anti-PD1 groups. Interestingly, the enhanced M1/M2 ratio in the combination group was not observed in our prior work with NextA.[13] Analysis of lymphoid cells shows a significant increase in CD8+ effector T-cells and effector memory (EM) cells in all of the treated groups compared to the control group (Figure 6D) in which the measured fold-increases were more significant in all the groups than prior studies performed with NextA. However, we only observed an increase in the percentage of CD8+ central memory (CM) cells with the Suprastat treated group, suggesting that it can enhance the effector memory function of CD8 T-cells for prolonged anti-tumor immune responses. Analysis of CD4+ T-cells did not show any significant changes in central memory (CM) or effector memory (EM) functions (Figure 6E). We also did not see a substantial change in immunosuppressive T-regs (Figure 6F). Further analysis of natural killer (NK) cells demonstrated an increase in the anti-PD1 group and combination group but did have a positive trend in the Suprastat group (Figure 6G), which was not observed in previous combination studies using NextA.[13] NK T-cells were significantly decreased in all treatment groups compared to the control group (Figure 6H), which may be speculated to a significant increase in CD8+ effector T-cells. Overall, the immune cell phenotyping indicates that Suprastat has improved immunomodulatory properties by decreasing pro-tumoral M2 macrophages and increasing the infiltration of anti-tumor CD8+ effector T-cells and memory cells relative to parent compound NextA. These factors are, in turn, likely

responsible for the enhanced immunomodulatory effects observed *in vivo* and the improved anti-tumor immune response in combination with anti-PD1 therapy.

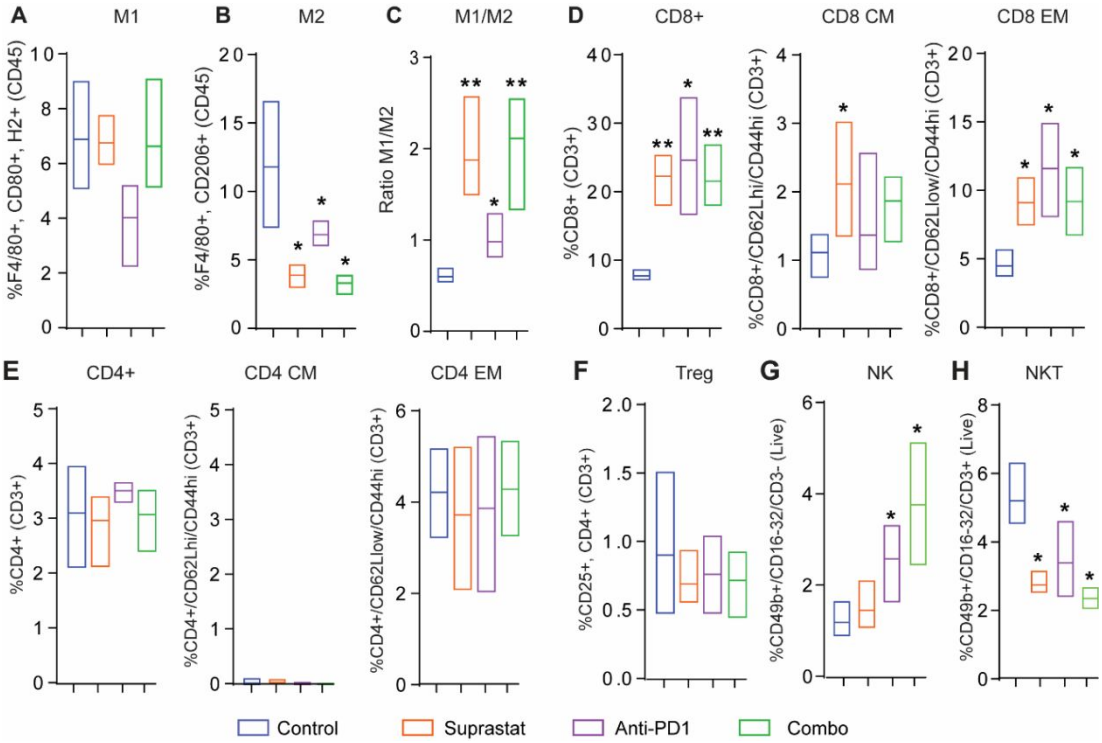

Figure 6. Suprastat has immunomodulatory properties in the tumor microenvironment. Macrophages (**A-C**), T-cells (**D-F**), and NK (**G** and **H**) cells were stained with cell surface markers and analyzed by multi-color flow cytometry.

X-ray crystallography. *In vitro* and *in vivo* characterization demonstrates that Suprastat is a highly selective HDAC6 inhibitor with significant antitumor effects through its immunomodulatory properties. To corroborate our *in-silico* models experimentally, we solved the crystal structure of the zHDAC6/Suprastat complex (PDB code 6TCY) to the resolution limit of 1.60 Å. The complex crystallized in the $P12_11$ monoclinic space group with two monomers in the asymmetric unit. There are no major conformational differences between the two monomers, as documented by the

RMSD of 0.12 Å for 314 corresponding Cα atoms. Interestingly though, the inhibitor can be modeled in two different conformations for each monomer in the asymmetric unit (Figure 7A and 7B). In the first and more populated inhibitor conformation, monodentate coordination is observed for the zinc atom with the hydroxamate N–O^- group with a Zn^{2+}--O^- distance of 2.24 Å. It is interesting to note that typical Zn^{2+}--O^- interatomic distances for monodentate HDAC6 complexes reported previously are shorter, falling into the range of 1.8 – 2.0 Å.[23-25, 46] At the same time, however, the Zn^{2+}--O^- interatomic distance in the NextA complex is 2.2 Å[23] that is virtually identical to the distance reported here. Clearly, the capping group of NextA (as well as its Suprastat derivative) might impose steric constraints on inhibitor positioning that leads to the somewhat atypical Zn^{2+} coordination. In the less populated conformation, the hydroxamate moiety coordinates with the active-site zinc ion in a bidentate fashion with interatomic distances of 2.25 and 2.34 Å for the hydroxamate N–O^- and C=O groups, respectively.

The phenyl rings of the linker fully overlap between the two conformers and are located in the internal tunnel delineated by the side chains of F583, F643, and H614 (Figure 7C). As for the capping group, the phenyl ring packs against a hydrophobic patch defined by the side chains of H463, P464, F583, and L712 of the L1-loop pocket (Figure 7D). As predicted by docking simulations, the positively charged aminomethyl group (pKa = 9.46, calculated by MarvinSketch Version 20.11) forms a salt bridge as well as a water-mediated hydrogen bond (3.0 Å) with the carboxylate group of D460 (Figure 7E). On the other hand, contrary to predictions, the hydroxybutyl group extends away

from the protein, and its distal hydroxyl group thus does not engage any residue of the HDAC6 rim directly but forms a solvent-mediated hydrogen bond with the side chain of N530 (Figure 7E). A 1.99 Å-resolution crystal structure of the zHDAC6/NextA complex was reported by the Matthias group in 2017 (PDB code 5G0I).[22] Superposition of the two complexes reveals virtually identical positions of the capping groups as well as surrounding HDAC6 residues, suggesting that our derivatization strategy did not elicit any (additional) conformational strain on the binding pose of the inhibitor (Figure 7F).

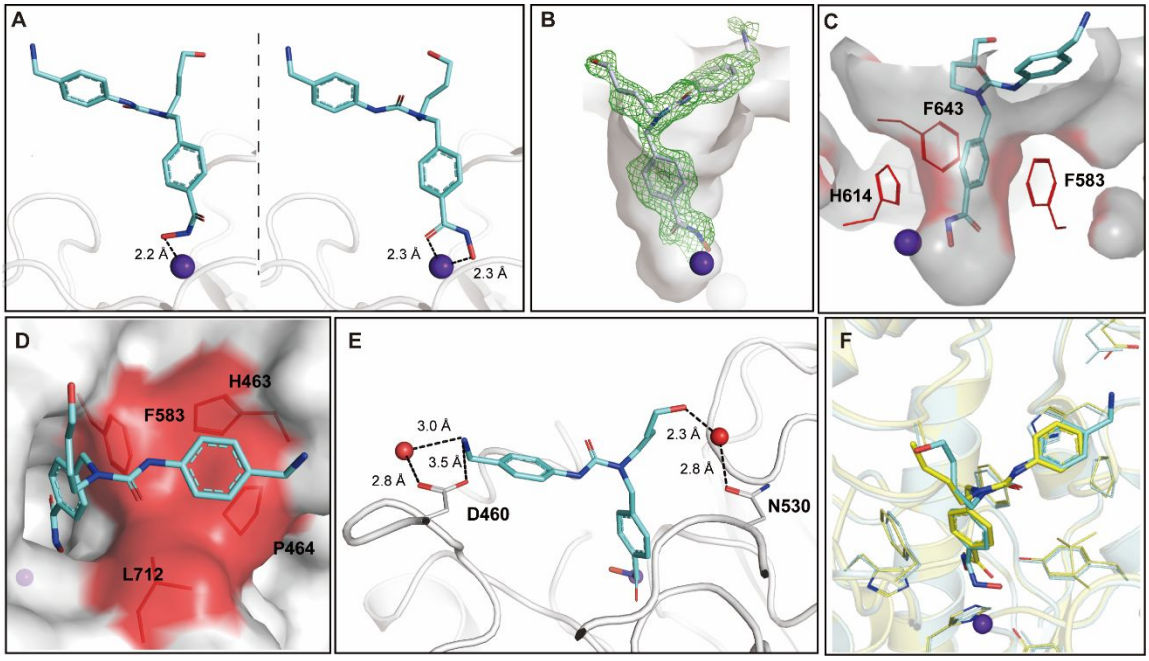

Figure 7. Crystal structure of the zHDAC6/Suprastat complex. (**A**) Both monodentate (left) and bidentate (right) coordination of the active-site Zn^{2+} ion is observed in the complex. (**B**) The omitted *Fo-Fc* difference electron density map for Suprastat is shown (green mesh) for the more prevalent monodentate binding mode (contoured at the 2σ level). (**C**, **D**) Non-polar interactions between the phenylhydroxamate function of Suprastat and residues delineating the internal tunnel (C); and the capping group and

the hydrophobic patch of the L1 loop (red surface representation; D). (**E**) Newly introduced polar/ionic contacts between the aminomethyl and hydroxylbutyl groups of Suprastat and D460 and N530, respectively (black dashed lines). (**F**) Superposition of binding modes of NextA (yellow, PDB code 5G0I) and Suprastat (cyan) documenting minimal structural differences between the two structures. Both structures were superposed on corresponding 320 Cα atoms with an rmsd of 0.192 Å. Inhibitors are shown in stick representation, carbon atoms are colored cyan (Suprastat) or yellow (NextA), oxygens are red, and nitrogens are blue. The catalytic zinc ion and water molecules are depicted as purple and red spheres, respectively.

Molecular dynamics simulations. X-ray crystallography is invaluable for the structure-assisted design of inhibitors yet, and crystal structures typically offer only a static snapshot of a single inhibitor binding pose disregarding the flexibility of inhibitors' functional moieties and protein residues. Moreover, the protein/inhibitor interaction pattern can also be influenced by crystallographic contacts. In solution, an inhibitor can interact only either with water molecules or the target protein. In crystals (due to crystal packing), functional groups (that stick outside HDAC6 pocket) can also interact "non-specifically" with neighboring molecules from the crystal. Consequently, the interaction pattern can be influenced by such contact and differ from the solution – thus, one does simulations to model contacts in solution. To explore the flexibility and ensemble of interactions between the Suprastat capping group and HDAC6, we carried out molecular dynamics (MD) simulations using the GROMACS software (2019). MD

simulation results (Figures 8A-C) indicate the ability of the hydroxybutyl chain to engage in two hydrogen-bond interactions with N530 (Figure 8A) and S531 (Figure 8C) at the rim of the catalytic pocket. At the same time, Figure 8B shows the transition state between each interaction. The direct frequency of contact (Figure 8D) determined for amino acids within the vicinity of the hydroxybutyl chain and the aminomethyl group indicates that the interactions with N530 and S531 repeatedly occurred during the entire simulation length (100 ns) (Supplementary Figures S3 and Video S1). On the contrary, direct contact between the ligand and D460 was not observed. There is an indirect interaction between the aminomethyl group and D460 mediated by two water molecules. Unlike both bidentate and monodentate hydroxamate-Zn^{2+} coordination modes were observed in the crystal complex, Suprastat mainly exhibited bidentate coordination mode with Zn^{2+} during the entire MD simulation process (Figures 2A-C and Supplementary Video S1). Overall, these findings suggest that the hydroxybutyl chain can directly engage in hydrogen bonding interactions with the side chains of N530 and S531, which were not observed in the zHDAC6/Suprastat crystal complex. It should be noted that in the case of the monoclinic crystal form reported here, the capping group of inhibitor comes to a short distance from a symmetry-related molecule, and both added polar functional groups engage with a symmetry-related HDAC6 molecule *via* solvent-mediated interactions. The observed crystallographic contacts may thus be responsible for differences in interaction patterns observed for the zHDAC6/Suprastat crystal complex as compared to MD simulations. Given the results from crystallographic studies and MD simulation, we conclude that Suprastat has a high

ability to interact with the residues D460, N530, and S531 that play crucial roles in regulating the tubulin deacetylation function of HDAC6.[22]

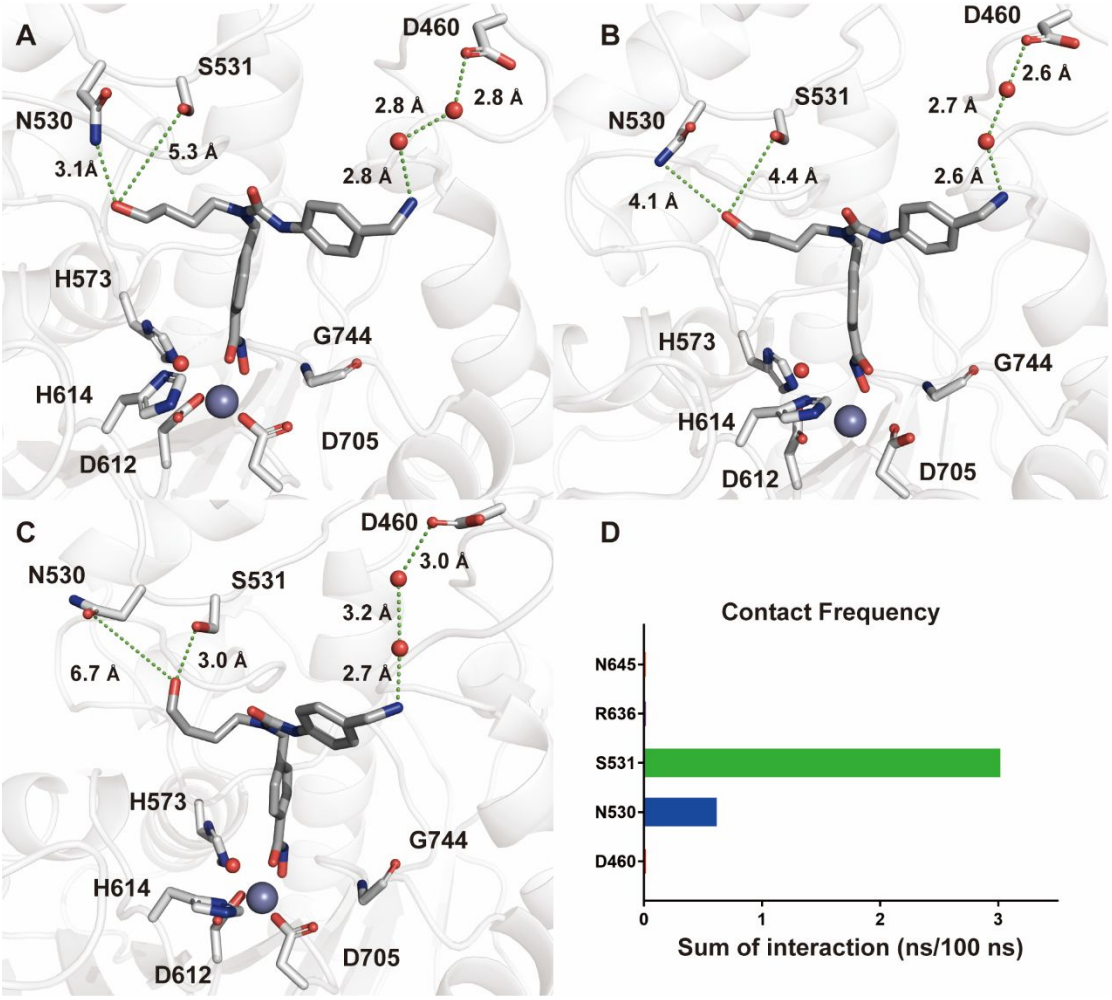

Figure 8. Representative poses of Suprastat bound to zHDAC6-CD2 catalytic pocket after Molecular Dynamics (MD) simulations. (**A**) The flexible hydroxylbutyl chain engages in H-bonding interaction with N530. (**B**) Transition state between each stable conformer. (**C**) H-bonding interaction between Suprastat and S531. (**A-C**) The aminomethyl group establishes a consistent water-mediated interaction with D460 during the MD simulation process. (**D**) Direct contact frequency between the hydroxylbutyl chain and the aminomethyl group of Suprastat and the amino acids at the rim of zHDAC6-CD2 along with the MD simulation. Carbon atoms are depicted as

grey. Nitrogen atoms are depicted as blue. Oxygen atoms are depicted as red. The Zn^{2+} ion is represented as a grey sphere. Water molecules are represented as red spheres. The protein is depicted in grey. Hydrogen-bonding interactions are depicted as green-dashed lines. Distances are reported in angstroms (Å). Images were generated in the PyMOL 2.1 software.

CONCLUSIONS

HDAC6 is unique among the histone deacetylases in possessing two functional catalytic domains and a C-terminal ubiquitin-binding domain.[47, 48] HDAC6 is predominantly cytosolic due to the presence of a nuclear export signal, and it thereby regulates the acetylation status of numerous cytosolic proteins. Among the many effects of HDAC6, it appears to possess immune-modulatory properties through regulation of the expression of immunosuppressive molecules such as IL-10 and PD-L1, thus leading to enhanced anti-tumor activity when combined with anti-PD1 immune checkpoint blockade therapy. For these reasons, there is an increasing interest in the identification of potent and highly selective HDAC6 inhibitors. Suprastat was rationally designed based on the crystal structure of Nexturastat A in complex with zHDAC6, wherein it was observed that the introduction of key functional groups would likely enhance HDAC6 potency and selectivity over other HDAC isoforms by establishing new hydrogen-bonding interactions with key residues in the HDAC6 pocket in addition to providing hydrophobic interactions between the cap and the rim region. In comparison with Nexturastat A and related analogs, Suprastat shows improved HDAC6 activity,

excellent isoform selectivity, and an enhanced ability to selectively elevate the levels of acetylated α-tubulin while having a less pronounced effect on histone acetylation in melanoma cells without cytotoxicity. The new polar functional groups on Suprastat decreases its lipophilicity, which leads to a higher lipophilic ligand efficiency and a lower plasma protein binding while maintaining good metabolic stability in different mediums. The *in vivo* combination therapy studies with an anti-PD1 antibody reveal that Suprastat significantly optimizes the therapeutic outcome through its promoted immunomodulatory properties relative to Nexturastat A. Finally, we have utilized x-ray crystallography and molecular dynamics simulations to support our premise that the incorporation of the aminomethyl and hydroxyl groups into the capping group can enlist additional hydrogen-bonding interactions with the key amino acids that regulate the α-tubulin deacetylation function of HDAC6. This work thus offers another example of the rational drug design of an improved HDAC6 inhibitor through the embellishment of hydrogen bonding interactions between the small molecule and its protein target. The work further underscores the ability of HDAC6 inhibitors to work in combination with anti-PD1 immune checkpoint blockade therapy to decrease tumor growth. To consider Suprastat as a drug candidate, genotoxicity studies (e.g., Ames test) will be further required to determine its mutagenic potential due to the hydroxamate moiety.[21] Moreover, PK/PD correlation studies of Suprastat will help understand the drug exposure and target engagement *in vivo* based on its promising antitumor efficacy, which we expect to perform in the next stage.

Experimental section.

Chemistry

General information. ^{1}H and ^{13}C NMR spectra were obtained on 400/101 and 500/126 MHz Bruker spectrometers, except where noted otherwise, using the solvent residual peak as the internal reference (chemical shifts: $CDCl_3$, δ 7.26/77.16 and DMSO-d_6, 2.50/39.52). The following abbreviations for multiplicities were used: s = singlet, d = doublet, t = triplet, q = quartet, m = multiplet, and br s = broad singlet. TLC plates (Merck silica gel 60 F_{254}, 250 μm thickness) were used to monitor reaction progress, and spots were visualized under UV (254 nm). High-resolution mass spectrometry (HRMS) was carried out on a Shimadzu IT-TOF instrument under the following conditions: column, ACE 3AQ (50 × 2.1 mm, id); mobile phase, 5 – 100% acetonitrile/water containing 0.1% formic acid at a flow rate of 0.5 mL/min for 4 min. Flash chromatography was performed on a Combi-Flash Rf system (Teledyne ISCO) with silica gel cartridges. Preparative HPLC was used in the purification of all final compounds using a Shimadzu preparative LC under the following conditions: column, ACE 5AQ (150 × 21.2 mm, id); mobile phase: 5 – 100% acetonitrile/water containing 0.05% TFA at a flow rate of 17 mL/min for 30 min; UV detection at 254 and 280 nm. Analytical HPLC was carried out on an Agilent 1260 series instrument under the following conditions: column, ACE 3 (150 × 4.6 mm, id); mobile phase, 5 – 100% acetonitrile/water containing 0.05% TFA at a flow rate of 1.0 mL/min for 25 min; UV detection at 254 nm. The purity of all tested compounds (TFA salts) for *in vitro* biological studies was >95%. The purity of Suprastat (HCl salt) *in vivo* studies

was >98%.

Phenyl (4-(((*tert*-Butoxycarbonyl)amino)methyl)phenyl)carbamate (2). To a stirred solution of *tert*-butyl (4-aminobenzyl)carbamate (**1**, 500 mg, 2.25 mmol) and K_2CO_3 (373 mg, 2.70 mmol) in acetone (15 mL) was added phenyl chloroformate (352 mg, 2.25 mmol) over 10 min. After stirring at room temperature for 2 h, the excess solid was filtered off. The filtrate was collected and concentrated under vacuum. The crude product was purified *via* flash chromatography (0 – 50% EtOAc/hexane) to afford **2** as a light yellow solid (700 mg, yield: 91%). ^{1}H NMR (400 MHz, $CDCl_3$) δ 7.41 – 7.37 (m, 4H), 7.25 – 7.16 (m, 6H), 4.86 (s, 1H), 4.27 (d, J = 4.7 Hz, 2H), 1.46 (s, 9H). ^{13}C NMR (101 MHz, $CDCl_3$) δ 156.1, 151.8, 150.7, 136.8, 134.6, 129.5 (2C), 128.4 (2C), 125.8, 121.8 (2C), 119.1 (2C), 79.7, 44.3, 28.5 (3C).

Methyl 4-(((4-Hydroxybutyl)amino)methyl)benzoate (4a). (i) A solution of 4-amino-1-butanol (0.28 mL, 6.10 mmol) and methyl-4-formylbenzoate (**3a**, 500 mg, 3.05 mmol) in EtOH (25 mL) was heated to reflux for 2 h. After cooling to room temperature, the resulting mixture was concentrated, and the crude product was used directly in the next step. (ii) To a stirred solution of the crude product in MeOH (50 mL), sodium borohydride (116 mg, 3.10 mmol) was added over 10 min at 0°C. The resulting mixture was allowed to warm to room temperature and stirred at room temperature for 2 h. Then the reaction was quenched with water, and the mixture was extracted with EtOAc (15 mL × 3). The combined organic layers were washed with brine, dried over Na_2SO_4, and concentrated under vacuum to afford **4a** as a colorless oil. The product was used directly in the next step without further purification (630 mg,

yield: 87% over two steps). ^{1}H NMR (400 MHz, $CDCl_3$) δ 7.98 (d, *J* = 8.1 Hz, 2H), 7.36 (d, *J* = 8.0 Hz, 2H), 3.88 (s, 3H), 3.82 (s, 2H), 3.58 (t, *J* = 5.0 Hz, 2H), 3.07 (br s, 2H, NH+OH), 2.67 (t, *J* = 5.4 Hz, 2H), 1.71 – 1.53 (m, 4H). ^{13}C NMR (101 MHz, $CDCl_3$) δ 167.0, 144.6, 130.0 (2C), 129.2, 128.3 (2C), 62.7, 53.6, 52.2, 49.4, 32.2, 28.4.

Methyl 4-((Butylamino)methyl)benzoate (4b) was synthesized from *n*-butylamine (0.31 mL, 6.10 mmol) and methyl-4-formylbenzoate (**3a**, 500 mg, 3.05 mmol) using a procedure similar to that described for the synthesis of **4a** and was obtained as a colorless oil (500 mg, yield: 74% over two steps. ^{1}H NMR (400 MHz, $CDCl_3$) δ 7.99 (d, *J* = 8.3 Hz, 2H), 7.39 (d, *J* = 8.3 Hz, 2H), 3.90 (s, 3H), 3.84 (s, 2H), 2.75 – 2.51 (m, 2H), 1.53 – 1.45 (m, 2H), 1.39 – 1.30 (m, 2H), 0.91 (t, *J* = 7.3 Hz, 3H). ^{13}C NMR (101 MHz, $CDCl_3$) δ 166.7, 145.9, 129.5 (2C), 128.5, 127.7 (2C), 53.5, 51.7, 49.0, 32.1, 20.3, 13.8.

4-(((4-Hydroxybutyl)amino)methyl)benzonitrile (**4c**) was synthesized from 4-amino-1-butanol (0.10 mL, 1.0 mmol) and 4-formylbenzonitrile (**3b**, 131 mg, 1.0 mmol) using a procedure similar to that described for the synthesis of **4a**. **4c** was obtained as a colorless oil (120 mg, yield: 59% over two steps) and used directly to the next step without characterization.

4-((4-Bromobenzyl)amino)butan-1-ol (**4d**) was synthesized from 4-amino-1-butanol (0.276 mL, 3 mmol) and 4-bromobenzaldehyde (**3c**, 550 mg, 3.0 mmol) using a procedure similar to that described for the synthesis of **4a**. **4d** was obtained as a colorless oil (0.53 g, yield: 68% over two steps) and used directly to the next step without characterization.

Methyl 4-((3-(4-(((*tert*-Butoxycarbonyl)amino)methyl)phenyl)-1-(4-hydroxybutyl)-ureido)methyl)benzoate (5a). To a stirred solution of **4a** (284 mg, 1.2 mmol) and **2** (350 mg, 1.0 mmol) in THF (10 mL) was added TEA (0.28 mL, 2.0 mmol). The resulting mixture was heated to reflux for 2 h. Then the reaction was cooled to room temperature and quenched with water (10 mL), and the mixture was extracted with EtOAc (10 mL × 3). The combined organic layers were washed with brine, dried over Na_2SO_4, and concentrated under vacuum. The residue was purified *via* flash chromatography (0 – 50% EtOAc/hexane) to afford **5a** as a colorless oil (420 mg, yield: 87%). ^{1}H NMR (400 MHz, $CDCl_3$) δ 7.94 (d, *J* = 8.1 Hz, 2H), 7.65 (br s, 1H), 7.29 (d, *J* = 8.1 Hz, 4H), 7.05 (d, *J* = 8.1 Hz, 2H), 5.10 (br s, 1H), 4.56 (s, 2H), 4.14 (s, 2H), 3.87 (s, 3H), 3.65 (d, *J* = 4.9 Hz, 2H), 3.53 (br s, 1H, OH), 3.31 (d, *J* = 6.2 Hz, 2H), 1.64 (s, 2H), 1.53 – 1.45 (m, 2H), 1.40 (s, 9H). ^{13}C NMR (101 MHz, $CDCl_3$) δ 167.0, 156.2, 156.1, 143.7, 138.7, 133.2, 130.0 (2C), 129.2, 127.8 (2C), 127.3 (2C), 120.3 (2C), 79.5, 62.5, 52.2, 49.9, 46.9, 44.1, 28.4 (3C), 27.6, 25.4.

Methyl 4-((3-(4-(((*tert*-Butoxycarbonyl)amino)methyl)phenyl)-1-butylureido)-methyl)benzoate (5b) was synthesized from **4b** (265 mg, 1.2 mmol) and **2** (350 mg, 1.0 mmol) using a procedure similar to that described for the synthesis of **5a** and was obtained as a colorless oil (400 mg, yield: 85%). ^{1}H NMR (400 MHz, $CDCl_3$) δ 7.98 (d, *J* = 8.2 Hz, 2H), 7.33 (d, *J* = 8.1 Hz, 2H), 7.24 (d, *J* = 8.4 Hz, 2H), 7.12 (d, *J* = 8.0 Hz, 2H), 6.52 (d, *J* = 6.6 Hz, 1H), 4.92 (s, 1H), 4.60 (s, 2H), 4.19 (d, *J* = 5.1 Hz, 2H), 3.89 (s, 3H), 3.40 – 3.23 (m, 2H, OH), 1.99 (t, *J* = 10.2 Hz, 1H), 1.59 (dd, *J* = 14.7, 7.2 Hz, 2H), 1.42 (s, 9H), 1.32 (dd, *J* = 14.9, 7.4 Hz, 2H), 0.91 (t, *J* = 7.3 Hz, 3H). ^{13}C

NMR (101 MHz, $CDCl_3$) δ 166.9, 156.0, 155.5, 143.3, 138.2, 133.7, 130.2 (2C), 129.4, 128.1 (2C), 127.1, 120.3 (2C), 79.4, 52.2, 50.4, 47.7, 44.2, 30.5, 28.5 (3C), 20.2, 13.9.

Methyl tert-Butyl (4-(3-(4-cyanobenzyl)-3-(4-hydroxybutyl)ureido)benzyl)carbamate (5c) was synthesized from **4c** (120 mg, 0.58 mmol) and **2** (200 mg, 0.58 mmol) using a procedure similar to that described for the synthesis of **5a** and was obtained as a colorless oil (80 mg, yield: 30%) ^{1}H NMR (400 MHz, $CDCl_3$) δ 7.80 (s, 1H), 7.57 (d, *J* = 7.9 Hz, 2H), 7.43 – 7.29 (m, 4H), 7.07 (d, *J* = 7.9 Hz, 2H), 5.01 (s, 1H), 4.58 (s, 2H), 4.16 (d, *J* = 4.5 Hz, 2H), 3.72 (s, 2H), 3.35 – 3.32 (m, 2H), 3.27 (br s, 1H), 1.69 (s, 2H), 1.54 (s, 2H), 1.42 (s, 9H). ^{13}C NMR (101 MHz, $CDCl_3$) δ 156.0, 155.9, 144.1, 138.6, 133.1, 132.3 (2C), 128.0 (2C), 127.7 (2C), 120.1 (2C), 118.7, 110.9, 79.4, 62.6, 49.8, 46.8, 44.1, 28.3 (3C), 27.0, 25.5.

tert-Butyl (4-(3-(4-bromobenzyl)-3-(4-hydroxybutyl)ureido)benzyl)carbamate (5d) was synthesized from **4d** (520 mg, 2 mmol) and **2** (680 mg, 2 mmol) using a procedure similar to that described for the synthesis of **5a** and was obtained as a colorless oil (960 mg, 95%). ^{1}H NMR (400 MHz, DMSO-d_6) δ 8.35 (s, 1H), 7.52 (d, *J* = 8.3 Hz, 2H), 7.37 (d, *J* = 8.1 Hz, 2H), 7.29 (br. t, 1H), 7.22 (d, *J* = 8.3 Hz, 2H), 7.08 (d, *J* = 8.1 Hz, 2H), 4.52 (s, 1H), 4.48 (br t, 2H), 4.03 (d, *J* = 5.6 Hz, 2H), 3.39 – 3.37 (m, 2H), 3.29 – 3.27 (m, 2H), 1.58 – 1.46 (m, 2H), 1.45 – 1.35 (m, 2H), 1.36 (s, 9H).

4-((3-(4-(Aminomethyl)phenyl)-1-(4-hydroxybutyl)ureido)methyl)-*N*-hydroxy-benzamide (6a). (i) In a round bottom flask, NaOH (68 mg, 1.69 mmol) was dissolved in 50% aqueous NH_2OH (0.7 mL, approx. 50 equiv.) at 0°C. A solution of **5a** (200 mg, 0.43 mmol) in 1:1 THF/MeOH (2/2 mL) was added dropwise, and stirring was

continued for 30 min while warming to room temperature. The solution was neutralized with 2N HCl and extracted with EtOAc (10 mL × 3). The combined organic layers were washed with brine, dried over Na_2SO_4, and concentrated under vacuum. The crude product was used directly in the next step without further purification. (ii) The crude intermediate was dissolved in THF (2 mL) followed by addition of TFA (3 mL) at room temperature. The resulting mixture was stirred at room temperature for 0.5 h, and then the excess solvent was removed under vacuum. The crude product was purified *via* preparative HPLC and lyophilized to afford **6a** as a white powder (62 mg, TFA salt, purity: 95%, yield: 29% over two steps). ^{1}H NMR (500 MHz, DMSO-d_6) δ 11.17 (br s, 1H), 8.51 (s, 1H), 8.07 (br s, 3H, NH_3^+), 7.72 (d, J = 8.7 Hz, 2H), 7.50 (d, J = 8.7 Hz, 2H), 7.32 (d, J = 6.6 Hz, 2H), 7.30 (d, J = 7.0 Hz, 2H), 4.61 (s, 2H), 3.94 (q, J = 5.8 Hz, 3H), 3.39 (t, J = 6.4 Hz, 2H), 3.33 (t, J = 7.4 Hz, 2H), 1.54 (ddd, J = 9.2, 6.4, 2.5 Hz, 2H), 1.41 (dt, J = 8.7, 6.5 Hz, 2H). ^{13}C NMR (126 MHz, DMSO-d_6) δ 164.0, 155.1, 142.2, 140.8, 131.4, 129.1 (2C), 127.01 (2C), 126.97 (2C), 126.9, 119.7 (2C), 60.6, 49.0, 46.3, 42.0, 29.4, 24.6. ESI HRMS calcd. for $C_{20}H_{25}N_4O_4$: $[M–H]^-$, m/z 385.1881; found: 385.1871.

4-((3-(4-(Aminomethyl)phenyl)-1-butylureido)methyl)-*N*-hydroxybenzamide (6b) was synthesized from **5b** (420 mg, 0.87 mmol) using a procedure similar to that described for the synthesis of **6a** and was obtained as a white solid (160 mg, TFA salt, purity: >99%, yield: 38% over two steps). ^{1}H NMR (400 MHz, DMSO-d_6) δ 11.17 (br s, 1H), 9.00 (br s, 1H), 8.48 (s, 1H), 8.01 (br s, 3H, NH_3^+), 7.72 (d, J = 8.2 Hz, 2H), 7.50 (d, J = 8.6 Hz, 2H), 7.32 (d, J = 6.4 Hz, 2H), 7.30 (d, J = 6.8 Hz, 2H), 4.61 (s, 2H),

3.93 (t, J = 5.6 Hz, 2H), 3.30 – 3.26 (m, 2H, overlapping with water peak), 1.53 – 1.40 (m, 2H), 1.31 – 1.16 (m, 2H), 0.86 (t, J = 7.3 Hz, 3H). ^{13}C NMR (126 MHz, DMSO-d_6) δ 164.0, 155.1, 142.2, 140.8, 131.4, 129.1 (2C), 127.0, 126.9 (4C), 119.8 (2C), 49.0, 46.2, 42.0, 29.9, 19.4, 13.8. ESI HRMS calcd. for $C_{20}H_{25}N_4O_3$: $[M–H]^-$, m/z 369.1932; found: 369.1923.

4-((3-(4-(Aminomethyl)phenyl)-1-(4-hydroxybutyl)ureido)methyl)benzoic acid (6d). To a stirred solution of **5a** (62 mg, 0.13 mmol) in THF/MeOH (1/1 mL) was added 1 N NaOH solution (1 mL). Then the resulting mixture was stirred at room temperature overnight. After the completion of the reaction detected by HPLC, the reaction was acidified by 2 N HCl, and extracted with THF (15 mL × 3). The combined organic extracts were washed with H_2O and brine, dried over Na_2SO_4, and concentrated under vacuum. The crude product was dissolved in THF (2 mL) followed by an addition of TFA (3 mL) at room temperature. The resulting mixture was stirred at room temperature for additional 0.5 h, then the excess solvent was removed under vacuum. The crude product was purified *via* preparative HPLC and lyophilized to afford **6d** as a white powder (40 mg, TFA salt, purity: 95%, yield: 63% over two steps). ^{1}H NMR (500 MHz, DMSO-d_6) δ 12.92 (br s, 1 H), 8.53 (s, 1H), 8.07 (br s, 3H, NH_3^+), 7.91 (d, J = 8.3 Hz, 2H), 7.51 (d, J = 8.6 Hz, 2H), 7.37 (d, J = 8.2 Hz, 2H), 7.30 (d, J = 8.7 Hz, 2H), 4.65 (s, 2H), 3.94 (q, J = 5.6 Hz, 2H), 3.39 (t, J = 6.4 Hz, 2H), 3.34 (t, J = 7.5 Hz, 2H), 1.54 (tt, J = 8.2, 6.3 Hz, 2H), 1.45 – 1.32 (m, 2H). ^{13}C NMR (126 MHz, DMSO-d_6) δ 167.2, 155.2, 144.2, 140.8, 129.5 (2C), 129.4, 129.1 (2C), 127.1 (2C), 127.0, 119.8 (2C), 60.6, 49.1, 46.4, 42.0, 29.4, 24.6. ESI HRMS calc. for $C_{20}H_{24}N_3O_4$: $[M–H]^-$, m/z

370.1772; found: 370.1769.

4-((3-(4-(Aminomethyl)phenyl)-1-(4-hydroxybutyl)ureido)methyl)benzamide (**6e**). To a stirred solution of **5c** (80 mg, 0.18 mmol) in DMSO (2 mL) were added K_2CO_3 (2.4 mg, 0.018 mmol) and H_2O_2 (30%, 0.2 mL) at room temperature. The resulting mixture was stirred for 5 h. After completion of the reaction, the solution was quenched with water (5 mL) and extracted with EtOAc (10 mL × 3). The organic layers were separated, washed with brine, dried over Na_2SO_4, and concentrated under vacuum. The crude product was dissolved in THF (2 mL) followed by an addition of TFA (3 mL) at room temperature. The resulting mixture was stirred at room temperature overnight, then the excess solvent was removed under vacuum. The crude product was purified *via* preparative HPLC and lyophilized to afford **6e** as a white powder (30 mg, TFA salt, purity: 98%, yield: 35% over two steps). ^{1}H NMR (500 MHz, DMSO-d_6) δ 8.51 (s, 1H), 8.06 (br s, 3H, NH_3^+), 7.92 (br s, 1H), 7.84 (d, J = 8.4 Hz, 2H), 7.51 (d, J = 8.6 Hz, 2H), 7.32 – 7.29 (m, 5H, one proton of $CONH_2$ overlaps with the signals from phenyl ring), 4.62 (s, 2H), 3.94 (q, J = 5.8 Hz, 3H), 3.39 (t, J = 6.4 Hz, 2H), 3.33 (t, J = 7.5 Hz, 2H), 1.54 (ddd, J = 12.1, 8.8, 6.4 Hz, 2H), 1.45 – 1.34 (m, 2H). ^{13}C NMR (126 MHz, DMSO-d_6) δ 167.6, 155.1, 142.3, 140.9, 133.0, 129.1 (2C), 129.0, 127.6 (2C), 126.8 (2C), 126.7, 119.7 (2C), 60.6, 49.0, 42.0, 29.4, 24.6. ESI HRMS calc. for $C_{20}H_{27}N_4O_3$: $[M+H]^+$, m/z 371.2078; found: 371.2087.

(4-((3-(4-(Aminomethyl)phenyl)-1-(4-hydroxybutyl)ureido)methyl)phenyl)boronic acid (**6f**). (i) To a stirred solution of **5d** (510 mg, 1.0 mmol), bis(pinacolato)diboron (280 mg, 1.1 mmol), and potassium acetate (290 mg, 3 mmol) in DMF (5 mL) was

added Pd(dppf)Cl_2 at room temperature under Argon atmosphere. After stirring at 80°C overnight, the reaction was cooled to room temperature, and the excess solid was filtered off. The filtrate was collected, quenched with saturated $NaHCO_3$ aqueous solution (20 mL), and extracted with EtOAc (20 mL × 3). The combined organic layers were washed with 10% LiCl aqueous solution, washed with brine (30 mL), dried over Na_2SO_4, and concentrated under vacuum. The crude was purified *via* flash chromatography (0 – 50% EtOAc/hexane) to afford the pinacol ester intermediate as a brown solid (0.25 g, yield: 44%). (ii) To a solution of the pinacol ester intermediate (240 mg, 0.44 mmol) in acetone/water (2:1, 9 mL) were added $NaIO_4$ (280 mg, 1.32 mmol) and NH_4OAc (100 mg, 1.32 mmol) at room temperature. After stirring at room temperature overnight, the reaction mixture was quenched with water and extracted with EtOAc (20 mL × 3). The combined organic layers were washed with brine (30 mL), dried over Na_2SO_4, and concentrated under vacuum. The crude product was used directly to the next step without further purification. (iii) The crude product was dissolved in THF (1 mL), followed by the addition of TFA (1 mL) at room temperature. The resulting mixture was stirred at room temperature for 0.5 h, and then the excess solvent was removed under vacuum. The crude product was purified *via* preparative HPLC and lyophilized to afford **6f** as a white powder (190 mg, TFA salt, purity: 99 %, yield: 39% over three steps). ^{1}H NMR (400 MHz, DMSO-d_6) δ 8.49 (s, 1H), 8.06 (br s, 3H, NH_3^+), 7.74 (d, J = 7.5 Hz, 2H), 7.50 (d, J = 8.2 Hz, 2H), 7.30 (d, J = 8.2 Hz, 2H), 7.21 (d, J = 7.6 Hz, 2H), 4.57 (s, 2H), 3.95 (s, 2H), 3.48 (t, J = 5.7 Hz, 2H), 3.31 (t, J = 6.7 Hz, 2H), 1.61 – 1.57 (m, 2H), 1.46 – 1.43 (m, 2H). ESI HRMS calc. for

$C_{19}H_{27}BN_3O_4$ $[M+H]^+$: *m/z* 372.2089, found: 372.2098.

Molecular docking studies. Docking models of ligand bound to HDAC6 were developed using the Molecular Operating Environment (MOE) computational suite's Builder utility. The energy minimization of ligands was conducted in the gas phase using the force field MMFF94X, followed by the Conformational Search protocol to generate structural-conformation databases. The zHDAC6-NextA crystal structure (PDB entry 5G0I; resolution: 1.99 Å) used as a template was obtained from the Protein Data Bank. The receptor preparation step was initiated with the removal of solvent except a single water molecule (HOH2316) close to the Zn^{2+} ion that was kept for modeling studies. Hydrogens were then placed, while ionization states were assigned throughout the system. Finally, ligands and binding sites were isolated in 3D, and then a molecular surface was drawn around the binding site to visualize the space available for docked ligands. Ligand placement employed the Alpha Triangle method with Affinity dG scoring generating 300 data points that were further refined using the induced fit method with GBVI/WSA dG scoring to obtain the top 50 docking results. The docking result of each ligand was analyzed for selection of the best docking pose, based on the score and reported X-ray structures. All renderings were then performed in PyMOL.

Ligand-protein binding free energy calculations were carried out in the Mopac 2016 package (Stewart Computational Chemistry). The free energy calculations were performed for the empty HDAC6-CD2 catalytic pocket (PDB code 5G0I), HDAC6-CD2 bound to Nexturastat A (PDB code 5G0I), and the HDAC6-CD2/Suprastat

complex (PDB code 6TCY). Free energy calculations for both isolated ligands (Nexturastat A and Suprastat) were also determined. The molecular geometries of each structure were optimized by the PM7 semiempirical method. Water molecules, zinc ions, and other ions were not considered for the calculation. A combination of molecular mechanics energies, polar and nonpolar solvation energies, and entropy were considered for the resulting binding free energy. The binding free energy calculations were performed considering both ligand and protein in aqueous solution using a dielectric constant (ε) of 78.4. The enthalpic (ΔH^0) and entropic (ΔS^0) contributes to the ΔG^0 value of NextA and Suprastat were also determined by the Gibbs free energy equation ($\Delta G^0 = \Delta H^0 - T\Delta S^0$).

Molecular dynamics simulation was performed in GROMACS 2019[49] (Fast Flexible and Free) for HDAC6-CD2/Suprastat complex (PDB code 6TCY). The simulation was carried out using the CHARMM force-field.[50, 51] The simulated system comprised the protein-ligand complex, the Zn^{2+} ion, a predefined water model (SPC)[52] as solvent, and counterions (Na^+ or Cl^- set to neutralize the overall system charge). The system was treated in a triclinic box with periodic boundary conditions specifying the shape and the size of the box as 10 Å distance from the box edges to any atom of the protein. We used a time step of 1 fs, and the short-range coulombic interactions were treated using a cut-off value of 8.0 Å, using the short-range method. The long-range coulombic interactions were handled *via* the smooth Particle Mesh Ewald method (PME).[53] Initially, the relaxation of the system was performed using both Steepest Descent and limited-memory Broyden-Fletcher-Goldfarb-Shanno algorithms in a hybrid manner.

The simulations were performed under the isothermal-isobaric ensemble (NPT) for 5 ns implementing the Berendsen thermostat and barostat methods. The temperature was maintained at 310 K throughout the simulation using the Nose-Hoover thermostat algorithm. The Martyna-Tobias-Klein barostat algorithm was employed to maintain 1 atm of pressure during calculations. After minimization and relaxation of the system, we proceeded with a single production step of 100 ns. The representative structure of Suprastat was selected by clustering the structures from the root-mean-square deviation (RSMD) values, using 0.5 Å as a cut-off. Figure S2 (Supporting Information) represents the variation of the RMSD values along with the simulation and the root mean square fluctuation (RMSF) for the protein backbone. Interactions and distances were determined using the trajectory analysis of GROMACS. The current geometric criteria for protein-ligand H-bonds are: i) a distance of 3.5 Å between donor (HBD) and acceptor (HBA) atoms; ii) an angle of ≥120° for the HBD between donor–hydrogen–acceptor atoms (D–H···A); and iii) an angle of ≥90° for the HBA between hydrogen-acceptor-bonded atom atoms (H···A–X). Similarly, protein-water or water-ligand H-bonds have; iv) a distance of 3.0 Å between HBD and HBA atoms; v) a donor angle of ≥110° between donor-hydrogen-acceptor atoms; vi) an acceptor angle of ≥ 90° between hydrogen-acceptor-bonded atom atoms. Non-specific hydrophobic interactions are defined by hydrophobic sidechains within 4.5 Å of aromatic or aliphatic carbons, and π-π interactions required two aromatic groups stacked face-to-face or face-to-edge, within 5.0 Å of distance.

Expression and purification of human HDACs 1-9 and 11. Large scale expression

of human HDACs was carried out in HEK293/T17 cells essentially as described previously.[54, 55] Briefly, transiently transfected cells were harvested three days post-transfection and the cell pellets resuspended in a lysis buffer (50 mM Tris, 150 mM NaCl, 10 mM KCl, 2 mM $MgCl_2$, 10% glycerol, 0.2% NP-40, and 2 Units/mL benzonase at pH 8) supplemented with a cocktail of protease inhibitors (Roche, Basel, Switzerland). Cells were lysed by sonication (30 W; 3 × 20 s) on ice, and the cell lysate cleared by centrifugation at 40,000 × *g* for 30 min at 4°C. Recombinant fusion HDAC proteins were purified *via* Strep-Tactin affinity chromatography (IBA, Göttingen, Germany) with the elution buffer comprising 50 mM HEPES, 100 mM NaCl, 50 mM KCl, 10% glycerol, and 3 mM desthiobiotin, pH 7.5. Purified proteins were concentrated to 1 mg/mL, aliquoted, flash-frozen in liquid nitrogen, and stored at –80°C until further use.

Determination of inhibitory activity against human HDACs 1-9 and 11. IC_{50} values in Table 1 were determined using a fluorescence-based assay with 10 μM Ac-GAK(Ac)-AMC (HDAC 1, 2, 3, 6) or 10 μM Boc-Lys(TFA)-AMC (HDAC 4, 5, 7, 8, 9, 11) as a substrate.[56] Briefly, individual HDACs were preincubated with dilution series of tested inhibitors in a 384-well plate in the total volume of 40 μL for 10 min at 37°C in a reaction buffer comprising 50 mM HEPES, 140 mM NaCl, 10 mM KCl, 1 mM TCEP, and 0.1% BSA at pH 7.4. Deacetylation reactions were started by the addition of 10 μL of a 10 μM substrate into the HDAC/inhibitor mixture. Following 30 min incubation at 37°C, the reaction was terminated by the addition of 25 μL of trypsin solution (4 mg/mL). Fluorescence development by trypsin was carried out at 37°C for

15 and 60 min for the Ac-GAK(Ac)-AMC and Boc-Lys(TFA)-AMC substrate, respectively. Released aminomethyl coumarin was quantified using a CLARIOstar fluorimeter with the excitation and emission wavelengths set to 365 nm and 440 nm, respectively. Non-linear regression analysis was employed to calculate IC_{50} values using the GraphPad Prism software. Fourteen-point IC_{50} curves were generated using a 3-fold inhibitor dilution series; inhibitor concentration ranges used: 100 μM – 63 pM for HDACs 1-5, 7-9, 11; and 3 μM – 1.88 pM for HDAC6. Reactions without the enzyme or the inhibitor were used to define 0% and 100% of the HDAC activity, respectively.

zHDAC6 expression and purification. The second catalytic domain of HDAC6 from *Danio rerio* (zHDAC6; amino acids 440 - 798) was expressed and purified essentially as described previously.[24] Briefly, the synthetic gene encoding HDAC6 was recombined into a Gateway expression plasmid in frame with the TEV-cleavable His-MBP N-terminal tag. The fusion protein was expressed in *E. coli* BL21-Codon Plus (DE3)-RIPL at 16°C overnight. The purification protocol comprised the HisTrap HP affinity step (GE Healthcare, Chicago, IL, USA), removal of the tag by the TEV protease, affinity purification on amylose resin (New England Biolabs, Ipswitch, MA, USA), ion-exchange chromatography on HiTrap Q sepharose (GE Healthcare), and size-exclusion chromatography on a HiLoad Superdex 75 pg column (GE Healthcare; mobile phase: 50 mM HEPES, 100 mM KCl, 5% glycerol, 1 mM TCEP, pH 7.5) as the final step. The purity of the final protein preparation was >98% as determined by SDS-PAGE, and purified zHDAC6-CD2 was concentrated to 10 mg/mL, aliquoted, flash-

frozen in liquid nitrogen, and stored at –80°C until further use. The IC_{50} value of NextA against zHDAC6 was determined to be 2.6 nM, which is comparable to its inhibitory affinity for hHDAC6 (IC_{50} = 1.6 nM) shown in Table 1.

Crystallization and data collection. The zHDAC6 stock solution was mixed with 1/20 volume of the Suprastat solution (80 mM in DMSO), and the crystallization droplets were prepared by combining 1 μL of the complex solution with 1 μL of a reservoir solution containing 19% PEG 3350 (Sigma Aldrich), 0.2 M KSCN (Hampton Research), and 0.1 M Bis-Tris (Sigma Aldrich) at pH 6.5. To bolster the nucleation step, droplets were streak-seeded using the seed stock prepared from crystals of the HDAC6/SAHA complex using a Crystal Crusher (Hampton Research). Crystals were grown by the hanging-drop vapor diffusion method at 283 K. Diffraction quality crystals were vitrified in liquid nitrogen from the mother liquor supplemented with 20% (*v/v*) glycerol. Data collection was carried out at 100 K on beamline 14.2 at the BESSY II synchrotron radiation source, Helmholtz-Zentrum Berlin, using Pilatus3 2M detector.[57] The data were processed using *Dials*,[58] including scaling using *dials.scale.* The data quality indicators were calculated using *Aimless* and *Auspex*;[59, 60] the data statistics are summarized in Table S2. The structure was solved by molecular replacement using *Phaser*[61] in the *CCP4 suite*[62] with structure PDB code 5EEK,[24] chain A as a search model. The procedure resulted in a solution with *R* of 36.6 and *LLG* of 22589. Structure refinement involved iterative cycles of the model building using *COOT*[63] according to $2mF_o$ - DF_c, and $2mF_o$ - DF_c Fourier maps and restrained refinement using *REFMAC5*.[64] R_{free} was used as a cross-validation statistic. The

presence of the ligand was confirmed using the Polder map.[65] The structure was validated using the *MolProbity* program suite[66] and a set of validation tools in *COOT*.[63]

Metabolic stability in body fluids and rat microsomes. Compounds were diluted to the initial concentration of 10 μM in the tested solution – PBS, simulated gastric fluid (SGF; 0.2 % NaCl, 0.7 % HCl, pH 1.2), or pooled human plasma (Innovative Research, Novi, MI, USA), all prewarmed to 37°C. Samples were incubated at 37°C, aliquots aspirated at defined time points, and samples were processed and analyzed as described below.

Rat liver microsomes were prepared according to a published protocol.[67] The final microsomal preparation was diluted to 10 mg/mL of total protein content in 50 mM Tris, pH 7.5 supplemented with 10 mM EDTA, and 20% glycerol, snap-frozen in liquid nitrogen, and stored at –80°C until further use. The metabolic activity of our in-house rat liver microsomes was virtually identical to commercially available preparations (rat liver microsomes, RTMCPL, Life Technologies, CA, USA; Supplementary Figure S4). Microsomes were diluted to the final concentration of 0.5 mg/mL (total protein) in 0.1 M potassium phosphate buffer, pH 7.4, and preincubated for 10 min at 37°C. Upon the addition of $MgCl_2$ (final concentration 1.25 mM), the tested compounds were added to the final concentration of 10 μM and the reaction started by the addition of NADPH solution (final concentration 1.8 mM). Aliquots were collected at defined time points, and samples were processed and analyzed as described below.

Plasma protein binding. An ultrafiltration (UF) protocol was used to determine compound binding to plasma proteins.[68] Tested compounds were diluted to 1 mM in

water, and this stock solution further diluted to the final concentration of 10 μM in PBS (non-specific binding control) or pooled human plasma. 200 μL of the tested solution was transferred to a Centrifuge ultrafiltration device (Merck Millipore, Burlington, MA, USA) and incubated at room temperature for 1 h. 50 μL of the sample was removed from the upper chamber (the input sample), and the assembled UF unit was centrifuged in a fixed angle rotor at 1,000 × *g* at room temperature for 5 min. 50 μL of the filtrate was mixed with the equivalent volume of either pooled human plasma (non-specific binding control samples) or PBS (plasma samples) to account for matrix effects.

The plasma binding was calculated according to the following formula:

Nonspecific binding (NSB):

$$NSB = (c_{B\_in} - c_{B\_fil})/c_{B\_in}$$

Free fraction (ff):

$$ff = c_{P\_fil}/[(1 - NSB) * c_{P\_in}]$$

Plasma bound (PB):

$$PB\ [\%] = 100 * (1 - ff)$$

where c_{B_in} is the input concentration of the compound in PBS, c_{B_fil} is the filtrate concentration from PBS samples, c_{P_in} is the input concentration in plasma samples, and c_{P_fil} is the concentration in the filtrate from plasma samples.

Sample processing and LC/MS-based quantification. Sample aliquots (stability or binding assays) were immediately mixed with three volumes of ice-cold acetonitrile containing Losartan as an internal standard (13.3 ng/mL), vortexed for 1 min, and centrifuged at 13,000 × *g* for 15 min. The supernatant was diluted with Milli-Q water

1:1 and compounds quantified by LC/MS-MS.

Mass spectrometry quantification was carried out using an MS-coupled HPLC system (Shimadzu LCMS-8040, Shimadzu, Kyoto, Japan) equipped with an API electrospray ion source. Analytes were separated on a Luna Omega Polar C18 1.6 µm, 100 Å column, 50 × 2.1 mm (Phenomenex, Torrance, CA, USA) using a gradient of 5-70% CH_3CN/H_2O containing 0.1% formic acid at a flow rate 0.6 mL/min over 4 min. Multiple reaction monitoring parameters were optimized for each analyte together with Losartan as an internal standard, and the predominant CID fragment was used for quantification. Data were analyzed using GraphPad Prism software (GraphPad Software, San Diego, CA, USA), where the ratio of the analyte signal over the Losartan signal was plotted against the incubation time, and data were fitted with an exponential one-phase decay equation to obtain a half-life of a tested compound.

Cell culture and antibodies. The SM1 murine melanoma cells were obtained from Dr. A. Ribas at the University of California, Los Angeles. WM164 human melanoma cells were obtained from ATCC. The cells were cultured in an incubator in RPMI 1640, 1% penicillin-streptomycin, and 10% fetal bovine serum at 37°C with 5% CO_2. HDAC inhibitors including **6a-c** and NextA were added at concentrations of 0.1 µM, 0.5 µM, 1 µM, 2.5 µM, 5 µM, and 10 µM, and the incubation was conducted overnight. For STAT3 phosphorylation assays, cells were pre-treated with or without HDAC6i (5 µM) for overnight followed by treatment with recombinant human IL-6 (Biolegend) for 20min. PBS was added as a control. RAW 264.7 macrophages were purchased from ATCC and cultured in DMEM medium supplemented with 10% FBS, 1% non-essential

amino acids, and 2-mercaptoethanol (50 μM). RAW macrophages were treated with 1 μM, 5 μM, and 10 μM of Suprastat overnight before collecting the lysates for immunoblot assay. Cytotoxicity assay was performed using CellTox Green (Promega, Cat#G8731) following the manufacturer's instructions, and fluorescence readings were obtained on Spectramax i3 (Molecular Devices) multimode plate reader at wavelengths EX 485nm and EM 520nm. SM1 cells were treated with compounds at various concentrations for 24 h to determine cytotoxicity.

Immunoblot analysis. The cells were harvested and lysed with RIPA buffer (ThermoScientific, 89900) containing protease and phosphatase inhibitors (ThermoScientific, 78440) by sonication in a Bioruptor (Diagenode) for 8 cycles of 30 s ON and 30 s OFF on high setting. To assess the expression of proteins, total protein samples were heat-denatured in SDS sample loading buffer, and 15-20 μg of protein was analyzed on 4-20% SDS-PAGE gels (Bio-Rad, 456-1093). Proteins were transferred onto low fluorescence PVDF membranes (Bio-Rad, 1704274) using a Trans-Blot Turbo transfer system (Bio-Rad). The membranes were blocked for 1 hour with Odyssey blocking buffer (Licor, 927-40000) followed by incubation with primary antibodies (1:1000 dilution) at 4°C. The membranes were washed in PBST buffer three times, followed by incubation with near-infrared fluorophore-conjugated secondary antibodies (1:10000 dilution) for 1 h at room temperature. The membranes were scanned on an Azure Biosystems C600 imager at near-infrared wavelengths. The images were analyzed and processed with Image Studio™ Lite software. The primary antibodies used are against phospho-STAT3 Y705 (Cell Signaling,9145), α-tubulin

(Cell Signaling, 3873), acetyl-α-tubulin (Cell Signaling, 3971), histone H3 (Cell Signaling, 3638), and acetyl-histone H3 (Cell Signaling, 9649).

Quantitative analysis of gene expression. Total RNA was isolated from cells following the manufacturer's instructions of QIAzol lysis reagent (Qiagen, 79306). RNA quantification was done using a NanoDrop One spectrophotometer (NanoDrop Technologies). Samples with absorbance at 260/280 nm ratios over 1.9 were used for cDNA synthesis with the iScript cDNA synthesis kit (Bio-Rad, 1708891). Synthesized cDNA from 1 μg of total RNA was diluted 1:10 with nuclease-free water. The quantitative PCR analysis was performed using iQ SYBR Green Supermix (Bio-Rad, 1708882) on a CFX96 real-time system (Bio-Rad). Gene expression analysis was performed using the $2^{-\Delta\Delta Ct}$ method, and target mRNA levels were normalized to *ACTB* expression. Cycling conditions were used as per the manufacturer's instructions. Single PCR product amplification was confirmed by melting curve analysis in all the experiments performed. The Mouse *IL10* QuantiTect Primer Assay (Qiagen, QT00106169) was purchased from Qiagen. The sequence of primers used in the analysis is as follows: mouse ACTB Forward: CATTGCTGACAGGATGCAGAAGG, Reverse: TGCTGGAAGGTGGACAGTGAGG were synthesized from Invitrogen.

Mice. Animal experiments involving mice were performed in accordance with the protocol (#A354) approved by the Institutional Care and Use Committee (IACUC) at The George Washington University. Forty C57BL/6 female mice were purchased from the Charles River Laboratories (Wilmington, Massachusetts, USA). *In vivo* studies were performed using SM1 tumor cells that were passaged *in vivo* from mouse to mouse

for a minimum of five times before tumor implantation. Mice were injected subcutaneously with 1.0×10^6 *in vivo* passaged SM1 melanoma cells suspended in 100 μL phosphate-buffered saline (PBS) (Corning, 21-040-CV). The pre-treatment arm was started once the tumors were palpable, which was about 5 days post tumor implantation. Cages were randomly assigned to different treatment groups, and mice were treated with Suprastat, anti-PD1 antibody, or vehicle control. Control mice were injected intraperitoneally with 100 μL PBS as vehicle control, a 15 mg/kg dose of anti-PD1 antibody (BioXcell, Clone RMP1-14), and 25 mg/kg of Suprastat. Mice were treated five days a week until tumors in the control group reached maximum size according to our IACUC protocol. Tumor volume measurements were taken on alternate days using caliper measurements and calculated using the formula $L \times W^2/2$. All animal studies were performed with consideration for toxicity, and we routinely monitored for early signs of toxicity. Emphasis was given to mortality, body weight, and food consumption. At the endpoint, a postmortem evaluation, including gross visual examination of organs such as the liver for hepatotoxicity, splenomegaly, and lung metastatic nodules, was done for each condition.

For macrophage isolation, bone marrow from 6-12 weeks old C57BL/6 mouse was used following an IACUC approved protocol. Briefly, femurs and tibia bones were isolated after removing the skeletal muscles. The bone marrow was flushed with RPMI complete medium supplemented with non-essential amino acids. A single-cell suspension of bone marrow was prepared with repeated pipetting and incubated with 20 ng/mL of mouse recombinant M-CSF (Biolegend) at 37°C for 4 days to differentiate

into macrophages. On Day 3, macrophages were pre-treated with 5μM Suprastat or vehicle. On Day 4, macrophages were treated with 5 μM Suprastat 1 h prior to polarization to M1 phenotype with 100 ng/mL of LPS (Sigma) and 20 ng/mL of recombinant mouse interferon-gamma (Biolegend).

Flow cytometry was performed following the protocol described previously.[13] Briefly, mice were euthanized following the IACUC protocol, and tumor cells were processed into a single cell suspension for analysis by flow cytometry with tumor digestion buffer. The following antibodies were used to stain cell surface markers expressed by different immune cells. All the antibodies were purchased from Biolegend (San Diego, CA) unless otherwise specified. Myeloid cell surface markers are as follows: Brilliant Violet 421™ anti-mouse/human CD11b (clone M1/70), APC anti-mouse CD80 (clone 16-10A1), PE/Cy7 anti-mouse CD206 (MMR) (clone C068C2), Brilliant Violet 650™ anti-mouse CD11c (clone N418), APC/Fire™ 750 anti-mouse CD45.2 (clone 104), PE anti-mouse CD123 (clone 5B11), Brilliant Violet 605™ anti-mouse Ly-6G/Ly-6C (Gr-1) (clone RB6-8C5), FITC anti-mouse H-2 (clone M1/42), Brilliant Violet 785™ anti-mouse F4/80 (clone BM8), and Alexa Fluor® 700 anti-mouse CD3 (clone 17A2). Lymphoid cell surface markers are as follows: PerCP/Cy5.5 anti-mouse CD3 (clone 17A2), Alexa Fluor® 488 anti-mouse CD4 (clone GK1.5), APC/Fire™ 750 anti-mouse CD8a (clone 53-6.7), Brilliant Violet 421™ anti-mouse CD25 (clone PC61), Brilliant Violet 785™ anti-mouse CD45.2 (clone 104), Brilliant Violet 605™ anti-mouse CD62L (clone MEL-14), Alexa Fluor® 647 anti-mouse CD127 (IL-7Rα) (clone A7R34), PE anti-mouse/human CD44 (clone IM7), PE/Cy7 anti-mouse CD49b (pan-

NK cells) (clone DX5), Brilliant Violet 421™ anti-mouse CD16/32 (clone 93), and PE anti-mouse 4-1BB (clone 17B5). Multi-color flow data acquisition was performed on BD Celesta, and data analysis was performed with FlowJo software (version 10.3). Statistical analyses were performed with GraphPad Prism Software (version 7.03).

ASSOCIATED CONTENT

Supporting Information

The Supporting Information is available free of charge on the ACS Publications website at DOI:

Supplementary results for cytotoxicity assay of **6a-c** along with NextA (Figure S1); supplementary results for immunoblot analysis of Suprastat's effects on α-tubulin acetylation in macrophages (Figure S2); supplementary figure and video for MD simulation (Figure S3 and Video S1); supplementary figure for liver microsomal stability test (Figure S4); supplementary data on the HDAC enzymatic assay of **6d-f** (Table S1); supplementary table for crystallization data collection and refinement statistics (Table S2).

^{1}H NMR spectra, ^{13}C NMR spectra, and HPLC purity reports for compounds **6a-c**.

Molecular formula strings including screening data.

Accession Codes

Atomic coordinates and corresponding structure factors for the zHDAC6-CD2/Suprastat complex have been deposited at the Protein Data Bank (PDB) as the 6TCY entry. Authors will release the atomic coordinates upon article publication.

AUTHOR INFORMATION

Corresponding Author

*(A.V.) E-mail: avillagra@gwu.edu. Phone: +1-202-994-9547.

*(A.P.K.) E-mail: alan@brightmindsbio.com. Phone: +1-773-793-5866.

*(C.B.): E-mail: Cyril.Barinka@ibt.cas.cz. Phone: +420-325-873-777.

ORCID

Sida Shen: 0000-0002-0295-2545

Maurício T. Tavares: 0000-0002-4400-7787

Guiping Zhang: 0000-0001-9818-4773

Cyril Bařinka: 0000-0003-2751-3060

Alan P. Kozikowski: 0000-0003-4795-5368

Alejandro Villagra: 0000-0001-9346-8355

Present Addresses

‡S.S.: Departments of Chemistry, Center for Molecular Innovation and Drug Discovery, and Center for Developmental Therapeutics, Northwestern University, Evanston, Illinois 60208, United States.

M.T.T.: Department of Molecular Medicine, Scripps Research, Jupiter, Florida 33458, United States.

Author Contributions

S.N. and S.S. contributed equally to this paper. A.V., A.P.K., and C.B. conceived the original idea, initiated the project, oversaw all the chemical, biological, crystallographic,

ADMET, as well as animal experimental designs/data analysis, and revised the manuscript. S.S. designed and synthesized compounds, oversaw all the experimental design, analyzed data, and wrote the manuscript with assistance from the other authors. S.N., M. H., and G.P. designed and performed all cellular and animal experimental designs, analyzed data, and contributed to the manuscript writing. J. Ptáček evaluated IC_{50} values of HDAC isoforms, generated ADMET data. J.S. and J. Pavlicek crystallized, solved, and refined the zHDAC6/Suprastat crystal complex. M.T.T and G.M.F. contributed to the molecular dynamics simulations. G.Z. contributed to the scale-up work of Suprastat.

Notes

The authors declare no competing financial interest.

ACKNOWLEDGMENTS

Funded by NIH R21 CA184612-01 and Melanoma Research Foundation CDA Grant Award (A.V.); NIH R01NS079183, R43HD093464, and R41AG058283 (A.P.K.). Additionally, this work was in part supported by the CAS (RVO: 86652036), the Czech Science Foundation (15-19640S), and project BIOCEV (CZ.1.05/1.1.00/02.0109) from the ERDF (C.B.). We would like to acknowledge the important technical contributions and advice of Kimberlyn Acklin, MS, SCYM (ASCP), at The George Washington University Flow Cytometry Core Facility and Bethany Rentz, RVT, at The George Washington University Office of Animal Research. We thank Petra Baranova and Barbora Havlinova for their excellent technical assistance and Lucia Motlova for help

with crystallization experiments. We also thank Dr. Werner Tueckmantel for proofreading the article and providing comments. We acknowledge the Helmholtz-Zentrum Berlin for the allocation of synchrotron radiation beamtime at the MX14.2 beamline and the support by the project CALIPSOplus (grant agreement 730872) from the EU Framework Programme for Research and Innovation HORIZON 2020 and CMS-Biocev ("Crystallization/Diffraction") supported by MEYS CR (LM2018127).

ABBREVIATIONS

Cbz, carboxylbenzyl; ADMET, absorption, distribution, metabolism, excretion, and toxicity; HPLC, high-performance liquid chromatography; rt, room temperature; TFA, trifluoroacetic acid; TEA, triethylamine; THF, tetrahydrofuran; DMF, *N*,*N*-dimethylformamide; DMSO, dimethyl sulfoxide; B_2pin_2, Bis(pinacolato)diboron; Pd(dppf)Cl_2, [1,1′-Bis(diphenylphosphino)ferrocene]-dichloropalladium (II); STAT3, Signal transducer and activator of transcription 3; IL-10, interleukin 10; PD-L1, programmed death-ligand 1; PD-1, programmed cell death-1.

REFERENCES

1. Zhao, S.; Xu, W.; Jiang, W.; Yu, W.; Lin, Y.; Zhang, T.; Yao, J.; Zhou, L.; Zeng, Y.; Li, H.; Li, Y.; Shi, J.; An, W.; Hancock, S. M.; He, F.; Qin, L.; Chin, J.; Yang, P.; Chen, X.; Lei, Q.; Xiong, Y.; Guan, K. L., Regulation of cellular metabolism by protein lysine acetylation. *Science* **2010**, *327*, 1000-1004.

2. Wang, Q.; Zhang, Y.; Yang, C.; Xiong, H.; Lin, Y.; Yao, J.; Li, H.; Xie, L.; Zhao,

W.; Yao, Y.; Ning, Z. B.; Zeng, R.; Xiong, Y.; Guan, K. L.; Zhao, S.; Zhao, G. P., Acetylation of metabolic enzymes coordinates carbon source utilization and metabolic flux. *Science* **2010**, *327*, 1004-1007.

3. Choudhary, C.; Weinert, B. T.; Nishida, Y.; Verdin, E.; Mann, M., The growing landscape of lysine acetylation links metabolism and cell signalling. *Nat. Rev. Mol. Cell Biol.* **2014**, *15*, 536-550.

4. Li, Y.; Seto, E., HDACs and HDAC inhibitors in cancer development and therapy. *Cold Spring Harb. Perspect Med.* **2016**, *6*, a026831.

5. Eckschlager, T.; Plch, J.; Stiborova, M.; Hrabeta, J., Histone deacetylase inhibitors as anticancer drugs. *Int. J. Mol. Sci.* **2017**, *18*, E1414.

6. Falkenberg, K. J.; Johnstone, R. W., Histone deacetylases and their inhibitors in cancer, neurological diseases and immune disorders. *Nat. Rev. Drug Discov.* **2014**, *13*, 673-691.

7. Matthias, P.; Yoshida, M.; Khochbin, S., HDAC6 a new cellular stress surveillance factor. *Cell Cycle* **2008**, *7*, 7-10.

8. Imai, Y.; Maru, Y.; Tanaka, J., Action mechanisms of histone deacetylase inhibitors in the treatment of hematological malignancies. *Cancer Sci.* **2016**, *107*, 1543-1549.

9. Shen, S.; Kozikowski, A. P., A patent review of histone deacetylase 6 inhibitors in neurodegenerative diseases (2014-2019). *Expert Opin. Ther. Pat.* **2020**, *30*, 121-136.

10. Rebe, C.; Ghiringhelli, F., STAT3, a master regulator of anti-tumor immune response. *Cancers* **2019**, *11*, E1280.

11. Cheng, F.; Lienlaf, M.; Wang, H. W.; Perez-Villarroel, P.; Lee, C.; Woan, K.; Rock-Klotz, J.; Sahakian, E.; Woods, D.; Pinilla-Ibarz, J.; Kalin, J.; Tao, J.; Hancock, W.; Kozikowski, A.; Seto, E.; Villagra, A.; Sotomayor, E. M., A novel role for histone deacetylase 6 in the regulation of the tolerogenic STAT3/IL-10 pathway in APCs. *J. Immunol.* **2014**, *193*, 2850-2862.

12. Lienlaf, M.; Perez-Villarroel, P.; Knox, T.; Pabon, M.; Sahakian, E.; Powers, J.; Woan, K.V.; Lee, C.; Cheng, F.; Deng, S.; Smalley, K.S.M.; Montecino, M.; Kozikowski, A.P.; Pinilla-Ibarz, J.; Sarnaik, A.; Seto, E.; Weber, J.; Sotomayor, E.M.; Villagra A., Essential role of HDAC6 in the regulation of PD-L1 in melanoma. *Mol. Oncol.* **2016**, *10*, 735-750.

13. Knox, T.; Sahakian, E.; Banik, D.; Hadley, M.; Palmer, E.; Noonepalle, S.; Kim, J.; Powers, J.; Gracia-Hernandez, M.; Oliveira, V.; Cheng, F.; Chen, J.; Barinka, C.; Pinilla-Ibarz, J.; Lee, N. H.; Kozikowski, A.; Villagra, A., Selective HDAC6 inhibitors improve anti-PD-1 immune checkpoint blockade therapy by decreasing the anti-inflammatory phenotype of macrophages and down-regulation of immunosuppressive proteins in tumor cells. *Sci. Rep.* **2019**, *9*, 6136.

14. Butler, K. V.; Kalin, J.; Brochier, C.; Vistoli, G.; Langley, B.; Kozikowski, A. P., Rational design and simple chemistry yield a superior, neuroprotective HDAC6 inhibitor, tubastatin A. *J. Am. Chem. Soc.* **2010**, *132*, 10842-10846.

15. Kalin, J. H.; Bergman, J. A., Development and therapeutic implications of selective histone deacetylase 6 inhibitors. *J. Med. Chem.* **2013**, *56*, 6297-6313.

16. De Vreese, R.; D'Hooghe, M., Synthesis and applications of benzohydroxamic

acid-based histone deacetylase inhibitors. *Eur. J. Med. Chem.* **2017**, *135*, 174-195.

17. Wang, X. X.; Wan, R. Z.; Liu, Z. P., Recent advances in the discovery of potent and selective HDAC6 inhibitors. *Eur. J. Med. Chem.* **2018**, *143*, 1406-1418.

18. Faria Freitas, M.; Cuendet, M.; Bertrand, P., HDAC inhibitors: a 2013-2017 patent survey. *Expert Opin. Ther. Pat.* **2018**, 28, 365-381.

19. Flipo, M.; Charton, J.; Hocine, A.; Dassonneville, S.; Deprez, B.; Deprez-Poulain, R., Hydroxamates: relationships between structure and plasma stability. *J. Med. Chem.* **2009**, *52*, 6790-6802.

20. Kozikowski, A. P.; Shen, S.; Pardo, M.; Tavares, M. T.; Szarics, D.; Benoy, V.; Zimprich, C. A.; Kutil, Z.; Zhang, G.; Barinka, C.; Robers, M. B.; Van Den Bosch, L.; Eubanks, J. H.; Jope, R. S., Brain penetrable histone deacetylase 6 inhibitor SW-100 ameliorates memory and learning impairments in a mouse model of Fragile X syndrome. *ACS Chem. Neurosci.* **2019**, *10*, 1679-1695.

21. Shen, S.; Kozikowski, A. P., Why hydroxamates may not be the best histone deacetylase inhibitors--What some may have forgotten or would rather forget? *ChemMedChem* **2016**, *11*, 15-21.

22. Miyake, Y.; Keusch, J. J.; Wang, L.; Saito, M.; Hess, D.; Wang, X.; Melancon, B. J.; Helquist, P.; Gut, H.; Matthias, P., Structural insights into HDAC6 tubulin deacetylation and its selective inhibition. *Nat. Chem. Biol.* **2016**, *12*, 748-754.

23. Porter, N. J.; Mahendran, A.; Breslow, R.; Christianson, D. W., Unusual zinc-binding mode of HDAC6-selective hydroxamate inhibitors. *Proc. Natl. Acad. Sci. U. S. A.* **2017**, *114*, 13459-13464.

24. Hai, Y.; Christianson, D. W., Histone deacetylase 6 structure and molecular basis of catalysis and inhibition. *Nat. Chem. Biol.* **2016**, *12*, 741-747.

25. Porter, N. J.; Osko, J. D.; Diedrich, D.; Kurz, T.; Hooker, J. M.; Hansen, F. K.; Christianson, D. W., Histone deacetylase 6-selective inhibitors and the influence of capping groups on hydroxamate-zinc denticity. *J. Med. Chem.* **2018**, *61*, 8054-8060.

26. Shen, S.; Hadley, M.; Ustinova, K.; Pavlicek, J.; Knox, T.; Noonepalle, S.; Tavares, M. T.; Zimprich, C. A.; Zhang, G.; Robers, M. B.; Barinka, C.; Kozikowski, A. P.; Villagra, A., Discovery of a new isoxazole-3-hydroxamate-based histone deacetylase 6 inhibitor SS-208 with antitumor activity in syngeneic melanoma mouse models. *J. Med. Chem.* **2019**, *62*, 8557-8577.

27. Vogerl, K.; Ong, N.; Senger, J.; Herp, D.; Schmidtkunz, K.; Marek, M.; Muller, M.; Bartel, K.; Shaik, T. B.; Porter, N. J.; Robaa, D.; Christianson, D. W.; Romier, C.; Sippl, W.; Jung, M.; Bracher, F., Synthesis and biological investigation of phenothiazine-based benzhydroxamic acids as selective histone deacetylase 6 inhibitors. *J. Med. Chem.* **2019**, *62*, 1138-1166.

28. Shen, S.; Svoboda, M.; Zhang, G.; Cavasin, M. A.; Motlova, L.; McKinsey, T. A.; Eubanks, J. H.; Barinka, C.; Kozikowski, A. P., Structural and in vivo characterization of Tubastatin A, a widely used histone deacetylase 6 inhibitor. *ACS Med. Chem. Lett.* **2020**, *11*, 706-712.

29. Osko, J. D.; Porter, N. J.; Narayana Reddy, P. A.; Xiao, Y. C.; Rokka, J.; Jung, M.; Hooker, J. M.; Salvino, J. M.; Christianson, D. W., Exploring structural determinants of inhibitor affinity and selectivity in complexes with histone deacetylase 6. *J. Med.*

Chem. **2020**, *63*, 295-308.

30. Bhatia, S.; Krieger, V.; Groll, M.; Osko, J. D.; Ressing, N.; Ahlert, H.; Borkhardt, A.; Kurz, T.; Christianson, D. W.; Hauer, J.; Hansen, F. K., Discovery of the first-in-class dual histone deacetylase-proteasome inhibitor. *J. Med. Chem.* **2018**, *61*, 10299-10309.

31. Osko, J. D.; Christianson, D. W., Structural determinants of affinity and selectivity in the binding of inhibitors to histone deacetylase 6. *Bioorg. Med. Chem. Lett.* **2020**, *30*, 127023.

32. Vergani, B.; Sandrone, G.; Marchini, M.; Ripamonti, C.; Cellupica, E.; Galbiati, E.; Caprini, G.; Pavich, G.; Porro, G.; Rocchio, I.; Lattanzio, M.; Pezzuto, M.; Skorupska, M.; Cordella, P.; Pagani, P.; Pozzi, P.; Pomarico, R.; Modena, D.; Leoni, F.; Perego, R.; Fossati, G.; Steinkuhler, C.; Stevenazzi, A., Novel benzohydroxamate-based potent and selective histone deacetylase 6 (HDAC6) inhibitors bearing a pentaheterocyclic scaffold: Design, synthesis, and biological evaluation. *J. Med. Chem.* **2019**, *62*, 10711-10739.

33. Bergman, J. A.; Woan, K.; Perez-Villarroel, P.; Villagra, A.; Sotomayor, E. M.; Kozikowski, A. P., Selective histone deacetylase 6 inhibitors bearing substituted urea linkers inhibit melanoma cell growth. *J. Med. Chem.* **2012**, *55*, 9891-9899.

34. Woan, K. V.; Lienlaf, M.; Perez-Villaroel, P.; Lee, C.; Cheng, F.; Knox, T.; Woods, D. M.; Barrios, K.; Powers, J.; Sahakian, E.; Wang, H. W.; Canales, J.; Marante, D.; Smalley, K. S. M.; Bergman, J.; Seto, E.; Kozikowski, A.; Pinilla-Ibarz, J.; Sarnaik, A.; Celis, E.; Weber, J.; Sotomayor, E. M.; Villagra, A., Targeting histone deacetylase 6

mediates a dual anti-melanoma effect: Enhanced antitumor immunity and impaired cell proliferation. *Mol. Oncol.* **2015**, *9*, 1447-1457.

35. Sixto-Lopez, Y.; Bello, M.; Correa-Basurto, J., Structural and energetic basis for the inhibitory selectivity of both catalytic domains of dimeric HDAC6. *J. Biomol. Struct. Dyn.* **2019**, *37*, 4701-4720.

36. Tavares, M. T.; Shen, S.; Knox, T.; Hadley, M.; Kutil, Z.; Barinka, C.; Villagra, A.; Kozikowski, A. P., Synthesis and pharmacological evaluation of selective histone deacetylase 6 inhibitors in melanoma models. *ACS Med. Chem. Lett.* **2017**, *8*, 1031-1036.

37. Jones, P.; Altamura, S.; De Francesco, R.; Paz, O. G.; Kinzel, O.; Mesiti, G.; Monteagudo, E.; Pescatore, G.; Rowley, M.; Verdirame, M.; Steinkuhler, C., A novel series of potent and selective ketone histone deacetylase inhibitors with antitumor activity in vivo. *J. Med. Chem.* **2008**, *51*, 2350-2353.

38. Kinzel, O.; Llauger-Bufi, L.; Pescatore, G.; Rowley, M.; Schultz-Fademrecht, C.; Monteagudo, E.; Fonsi, M.; Gonzalez Paz, O.; Fiore, F.; Steinkuhler, C.; Jones, P., Discovery of a potent class I selective ketone histone deacetylase inhibitor with antitumor activity in vivo and optimized pharmacokinetic properties. *J. Med. Chem.* **2009**, *52*, 3453-3456.

39. Bresciani, A.; Ontoria, J. M.; Biancofiore, I.; Cellucci, A.; Ciammaichella, A.; Di Marco, A.; Ferrigno, F.; Francone, A.; Malancona, S.; Monteagudo, E.; Nizi, E.; Pace, P.; Ponzi, S.; Rossetti, I.; Veneziano, M.; Summa, V.; Harper, S., Improved selective Class I HDAC and novel selective HDAC3 inhibitors: beyond hydroxamic acids and

benzamides. *ACS Med. Chem. Lett.* **2019**, *10*, 481-486.

40. Hai, Y.; Shinsky, S. A.; Porter, N. J.; Christianson, D. W., Histone deacetylase 10 structure and molecular function as a polyamine deacetylase. *Nat. Commun.* **2017**, *8*, 15368.

41. Daina, A.; Michielin, O.; Zoete, V., SwissADME: a free web tool to evaluate pharmacokinetics, drug-likeness and medicinal chemistry friendliness of small molecules. *Sci. Rep.* **2017**, *7*, 42717.

42. Johnson, T. W.; Gallego, R. A.; Edwards, M. P., Lipophilic efficiency as an important metric in drug design. *J. Med. Chem.* **2018**, *61*, 6401-6420.

43. Hopkins, A. L.; Groom, C. R.; Alex, A., Ligand efficiency: a useful metric for lead selection. *Drug Discov. Today* **2004**, *9*, 430-431.

44. Koya, R. C.; Mok, S.; Otte, N.; Blacketor, K. J.; Comin-Anduix, B.; Tumeh, P. C.; Minasyan, A.; Graham, N. A.; Graeber, T. G.; Chodon, T.; Ribas, A., BRAF inhibitor vemurafenib improves the antitumor activity of adoptive cell immunotherapy. *Cancer Res.* **2012**, *72*, 3928-3937.

45. O'Donnell, J. S.; Long, G. V.; Scolyer, R. A.; Teng, M. W.; Smyth, M. J., Resistance to PD1/PDL1 checkpoint inhibition. *Cancer Treat Rev.* **2017**, *52*, 71-81.

46. Porter, N. J.; Wagner, F. F.; Christianson, D. W., Entropy as a driver of selectivity for inhibitor binding to histone deacetylase 6. *Biochemistry* **2018**, *57*, 3916-3924.

47. Seigneurin-Berny, D.; Verdel, A.; Curtet, S.; Lemercier, C.; Garin, J.; Rousseaux, S.; Khochbin, S., Identification of components of the murine histone deacetylase 6 complex: link between acetylation and ubiquitination signaling pathways. *Mol. Cell*

Biol. **2001**, *21*, 8035-8044.

48. Boyault, C.; Sadoul, K.; Pabion, M.; Khochbin, S., HDAC6, at the crossroads between cytoskeleton and cell signaling by acetylation and ubiquitination. *Oncogene* **2007**, *26*, 5468-5476.

49. Van Der Spoel, D.; Lindahl, E.; Hess, B.; Groenhof, G.; Mark, A. E.; Berendsen, H. J., GROMACS: fast, flexible, and free. *J. Comput. Chem.* **2005**, *26*, 1701-1718.

50. Vanommeslaeghe, K.; Hatcher, E.; Acharya, C.; Kundu, S.; Zhong, S.; Shim, J.; Darian, E.; Guvench, O.; Lopes, P.; Vorobyov, I.; Mackerell, A. D., Jr., CHARMM general force field: A force field for drug-like molecules compatible with the CHARMM all-atom additive biological force fields. *J. Comput. Chem.* **2010**, *31*, 671-690.

51. Vermaas, J. V.; Hardy, D. J.; Stone, J. E.; Tajkhorshid, E.; Kohlmeyer, A., TopoGromacs: automated topology conversion from CHARMM to GROMACS within VMD. *J. Chem. Inf. Model* **2016**, *56*, 1112-1116.

52. Bjelkmar, P.; Larsson, P.; Cuendet, M. A.; Hess, B.; Lindahl, E., Implementation of the CHARMM force field in GROMACS: analysis of protein stability effects from correction maps, virtual interaction sites, and water models. *J. Chem. Theory Comput.* **2010**, *6*, 459-466.

53. Darden, T.; York, D.; Pedersen, L., Particle mesh ewald - an N.Log(N) method for ewald sums in large systems. *J. Chem. Phys.* **1993**, *98*, 10089-10092.

54. Skultetyova, L.; Ustinova, K.; Kutil, Z.; Novakova, Z.; Pavlicek, J.; Mikesova, J.; Trapl, D.; Baranova, P.; Havlinova, B.; Hubalek, M.; Lansky, Z.; Barinka, C., Human

histone deacetylase 6 shows strong preference for tubulin dimers over assembled microtubules. *Sci. Rep.* **2017**, *7*, 11547.

55. Kutil, Z.; Novakova, Z.; Meleshin, M.; Mikesova, J.; Schutkowski, M.; Barinka, C., Histone deacetylase 11 is a fatty-acid deacylase. *ACS Chem. Biol.* **2018**, *13*, 685-693.

56. Wu, H.; Yang, K.; Zhang, Z.; Leisten, E.; Li, Z.; Xie, H.; Liu, J.; Smith, K. A.; Novakova, Z.; Barinka, C.; Tang, W., Development of multi-functional histone deacetylase 6 degraders with potent anti-myeloma activity. *J. Med. Chem.* **2019**, *62*, 7042-7057.

57. M. Gerlach, U. Mueller, M. S. Weiss, The MX beamlines BL14.1-3 at BESSY II. *J. Large-scale Res. Facilities* DOI: 10.17815/jlsrf-2-64.

58. Winter, G.; Waterman, D. G.; Parkhurst, J. M.; Brewster, A. S.; Gildea, R. J.; Gerstel, M.; Fuentes-Montero, L.; Vollmar, M.; Michels-Clark, T.; Young, I. D.; Sauter, N. K.; Evans, G., DIALS: implementation and evaluation of a new integration package. *Acta Crystallogr. D Struct. Biol.* **2018**, *74*, 85-97.

59. Evans, P. R., An introduction to data reduction: space-group determination, scaling and intensity statistics. *Acta Crystallogr. D Biol. Crystallogr.* **2011**, *67*, 282-292.

60. Thorn, A.; Parkhurst, J.; Emsley, P.; Nicholls, R. A.; Vollmar, M.; Evans, G.; Murshudov, G. N., AUSPEX: a graphical tool for X-ray diffraction data analysis. *Acta Crystallogr. D Struct. Biol.* **2017**, *73*, 729-737.

61. McCoy, A. J.; Grosse-Kunstleve, R. W.; Adams, P. D.; Winn, M. D.; Storoni, L. C.; Read, R. J., Phaser crystallographic software. *J. Appl. Crystallogr.* **2007**, *40*, 658-

674.

62. Winn, M. D.; Ballard, C. C.; Cowtan, K. D.; Dodson, E. J.; Emsley, P.; Evans, P. R.; Keegan, R. M.; Krissinel, E. B.; Leslie, A. G.; McCoy, A.; McNicholas, S. J.; Murshudov, G. N.; Pannu, N. S.; Potterton, E. A.; Powell, H. R.; Read, R. J.; Vagin, A.; Wilson, K. S., Overview of the CCP4 suite and current developments. *Acta Crystallogr. D Biol. Crystallogr.* **2011**, *67*, 235-242.

63. Emsley, P.; Lohkamp, B.; Scott, W. G.; Cowtan, K., Features and development of Coot. *Acta Crystallogr. D Biol. Crystallogr.* **2010**, *66*, 486-501.

64. Murshudov, G. N.; Vagin, A. A.; Dodson, E. J., Refinement of macromolecular structures by the maximum-likelihood method. *Acta Crystallogr. D Biol. Crystallogr.* **1997**, *53*, 240-255.

65. Liebschner, D.; Afonine, P. V.; Moriarty, N. W.; Poon, B. K.; Sobolev, O. V.; Terwilliger, T. C.; Adams, P. D., Polder maps: improving OMIT maps by excluding bulk solvent. *Acta Crystallogr. D Struct. Biol.* **2017**, *73*, 148-157.

66. Chen, V. B.; Arendall, W. B., 3rd; Headd, J. J.; Keedy, D. A.; Immormino, R. M.; Kapral, G. J.; Murray, L. W.; Richardson, J. S.; Richardson, D. C., MolProbity: all-atom structure validation for macromolecular crystallography. *Acta Crystallogr. D Biol. Crystallogr.* **2010**, *66*, 12-21.

67. Knights, K. M.; Stresser, D. M.; Miners, J. O.; Crespi, C. L., In vitro drug metabolism using liver microsomes. *Curr. Protoc. Pharmacol.* **2016**, *74*, 7.8.1.-7.8.24.

68. Barre, J.; Chamouard, J. M.; Houin, G.; Tillement, J. P., Equilibrium dialysis, ultrafiltration, and ultracentrifugation compared for determining the plasma-protein-

binding characteristics of valproic acid. *Clin. Chem.* **1985**, *31*, 60-64.

Table of Contents graphic

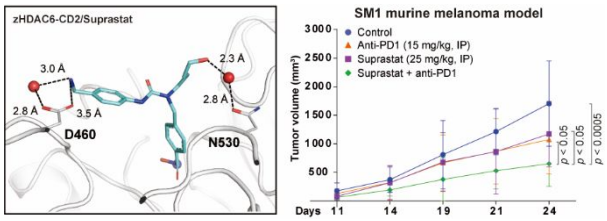

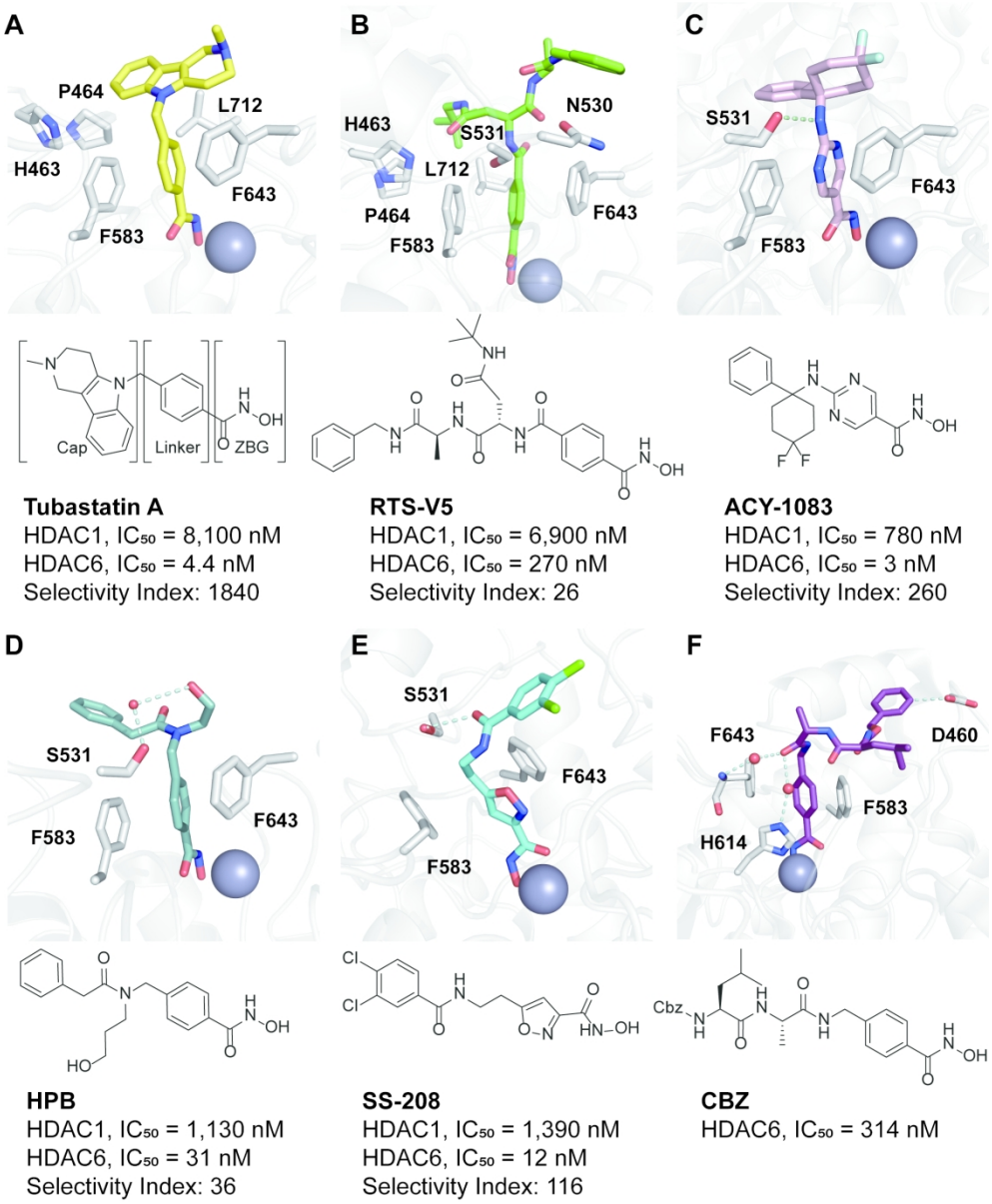
A
P464
L712
H463
F643
F583
B
H463
S531
N530
L712
P464
F643
F583
C
S531
F643
F583
Cap
Linker
ZBG
Tubastatin A
HDAC1, IC50 = 8,100 nM
HDAC6, IC50 = 4.4 nM
Selectivity Index: 1840
RTS-V5
HDAC1, IC50 = 6,900 nM
HDAC6, IC50 = 270 nM
Selectivity Index: 26
ACY-1083
HDAC1, IC50 = 780 nM
HDAC6, IC50 = 3 nM
Selectivity Index: 260
D
S531
F583
F643
E
S531
F643
F583
F
F643
D460
F583
H614
HPB
HDAC1, IC50 = 1,130 nM
HDAC6, IC50 = 31 nM
Selectivity Index: 36
SS-208
HDAC1, IC50 = 1,390 nM
HDAC6, IC50 = 12 nM
Selectivity Index: 116
CBZ
HDAC6, IC50 = 314 nM

Figure 1

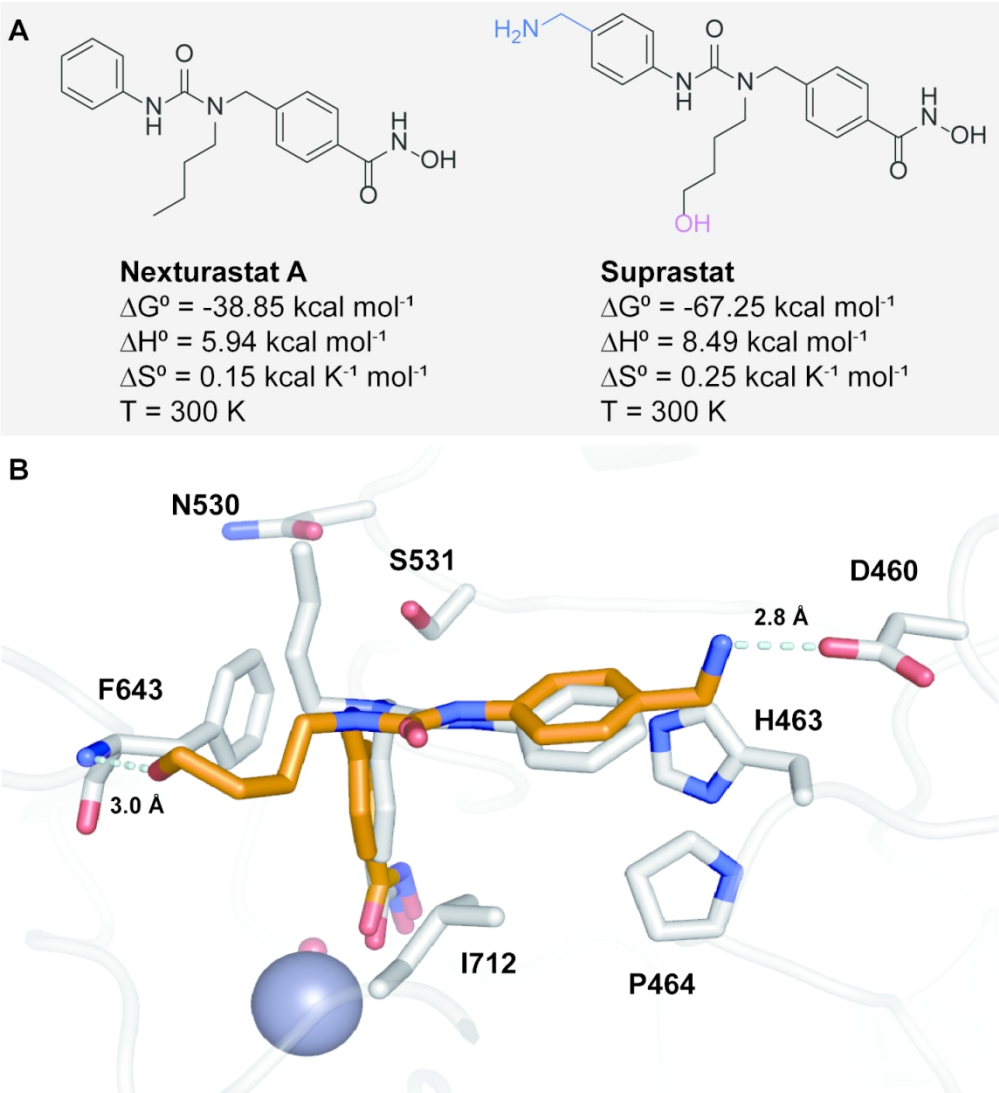
A
Nexturastat A
ΔG° = -38.85 kcal mol-1
ΔH° = 5.94 kcal mol-1
ΔS° = 0.15 kcal K-1 mol-1
T = 300 K
Suprastat
ΔG° = -67.25 kcal mol-1
ΔH° = 8.49 kcal mol-1
ΔS° = 0.25 kcal K-1 mol-1
T = 300 K
B
N530
S531
D460
2.8 Å
F643
H463
3.0 Å
I712
P464

Figure 2

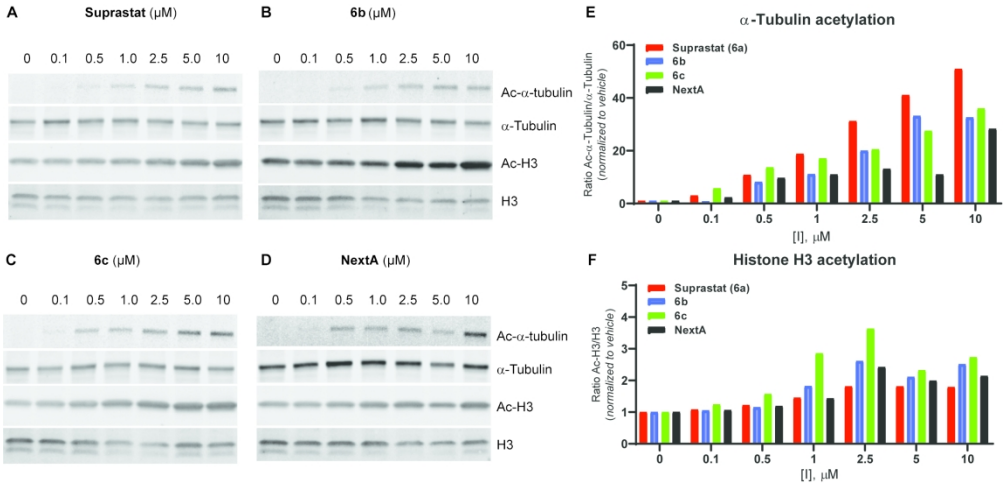
A
Suprastat (μM)
0 0.1 0.5 1.0 2.5 5.0 10
B
6b (μM)
0 0.1 0.5 1.0 2.5 5.0 10
Ac-α-tubulin
α-Tubulin
Ac-H3
H3
C
6c (μM)
0 0.1 0.5 1.0 2.5 5.0 10
D
NextA (μM)
0 0.1 0.5 1.0 2.5 5.0 10
Ac-α-tubulin
α-Tubulin
Ac-H3
H3
E
α-Tubulin acetylation
Suprastat (6a)
6b
6c
NextA
Ratio Ac-α-Tubulin/α-Tubulin (normalized to vehicle)
[I], μM
F
Histone H3 acetylation
Suprastat (6a)
6b
6c
NextA
Ratio Ac-H3/H3 (normalized to vehicle)
[I], μM

Figure 3

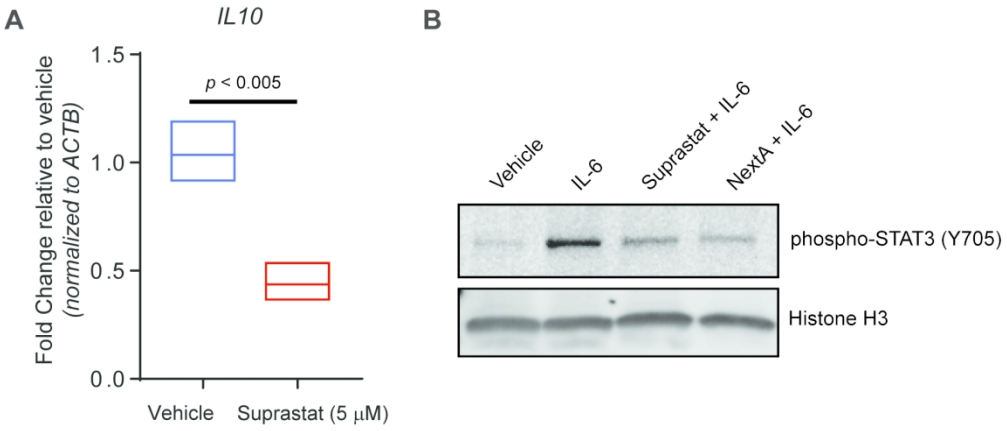
A
IL10
p < 0.005
Fold Change relative to vehicle
(normalized to ACTB)
1.5
1.0
0.5
0.0
Vehicle
Suprastat (5 μM)
B
Vehicle
IL-6
Suprastat + IL-6
NextA + IL-6
phospho-STAT3 (Y705)
Histone H3

Figure 4

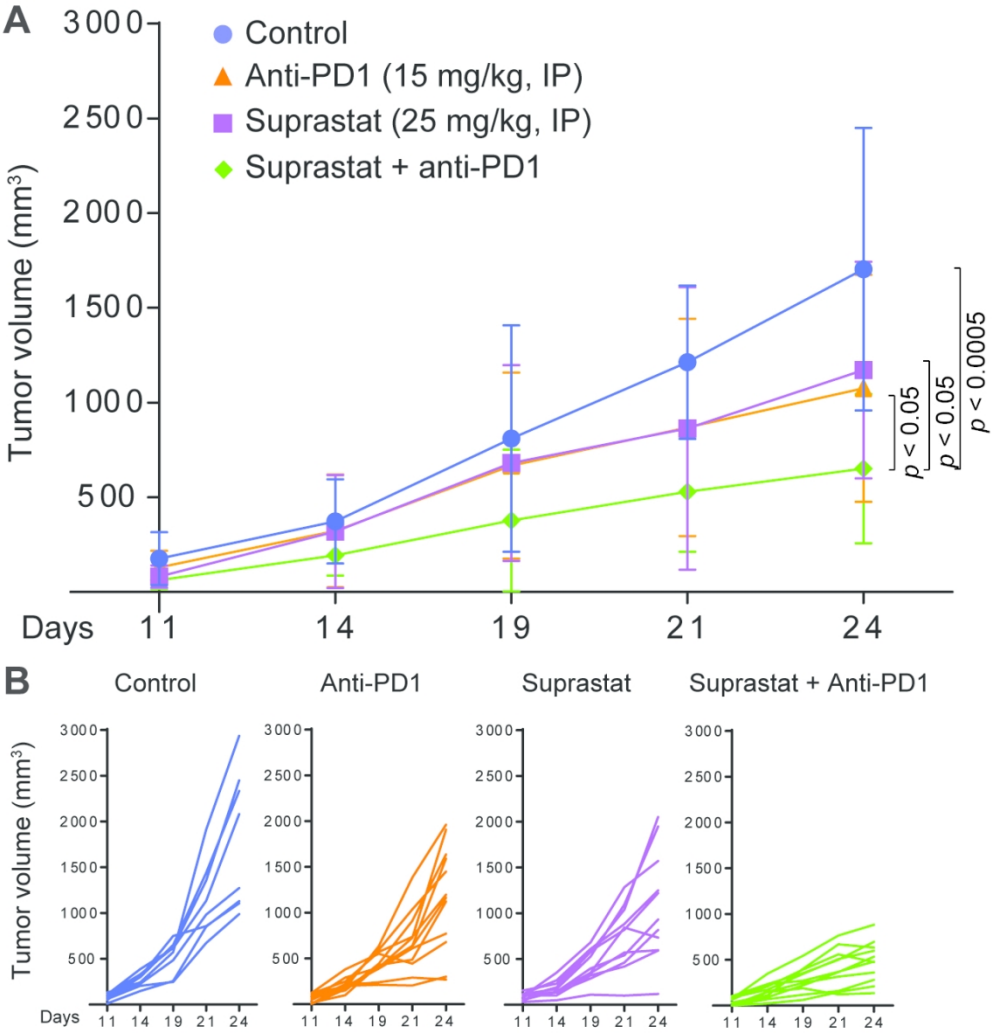
A
Control
Anti-PD1 (15 mg/kg, IP)
Suprastat (25 mg/kg, IP)
Suprastat + anti-PD1
Tumor volume (mm³)
3000
2500
2000
1500
1000
500
Days
11
14
19
21
24
p < 0.05
p < 0.05
p < 0.0005
B
Control
Anti-PD1
Suprastat
Suprastat + Anti-PD1
Tumor volume (mm³)
Days

Figure 5

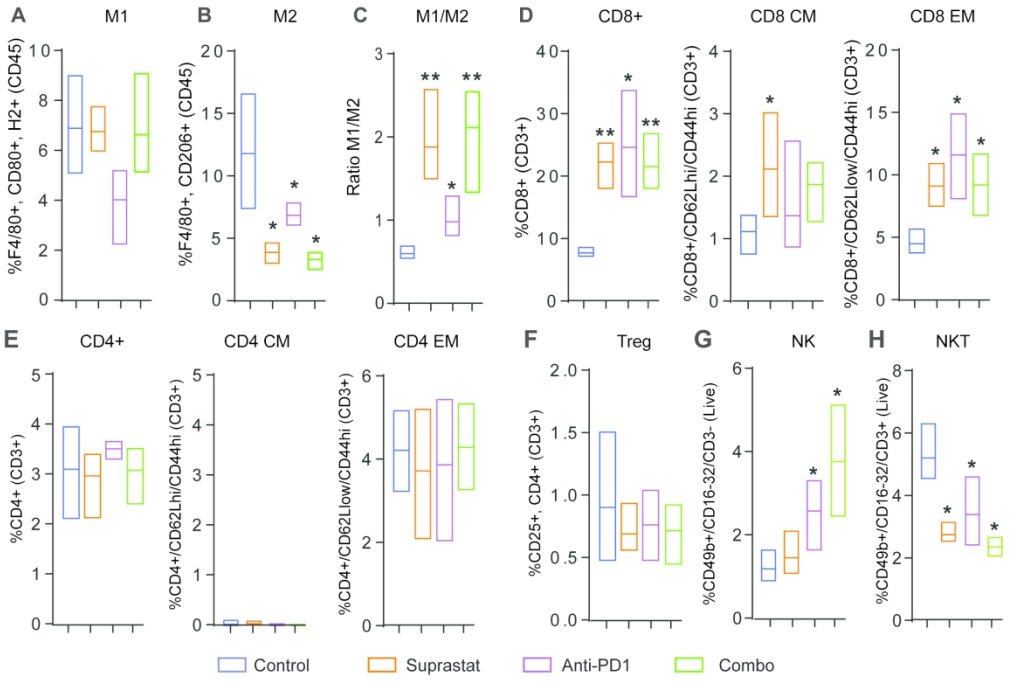
A
M1
%F4/80+, CD80+, H2+ (CD45)
B
M2
%F4/80+, CD206+ (CD45)
C
M1/M2
Ratio M1/M2
D
CD8+
%CD8+ (CD3+)
CD8 CM
%CD8+/CD62Lhi/CD44hi (CD3+)
CD8 EM
%CD8+/CD62Llow/CD44hi (CD3+)
E
CD4+
%CD4+ (CD3+)
CD4 CM
%CD4+/CD62Lhi/CD44hi (CD3+)
CD4 EM
%CD4+/CD62Llow/CD44hi (CD3+)
F
Treg
%CD25+, CD4+ (CD3+)
G
NK
%CD49b+/CD16-32/CD3- (Live)
H
NKT
%CD49b+/CD16-32/CD3+ (Live)
Control
Suprastat
Anti-PD1
Combo

Figure 6

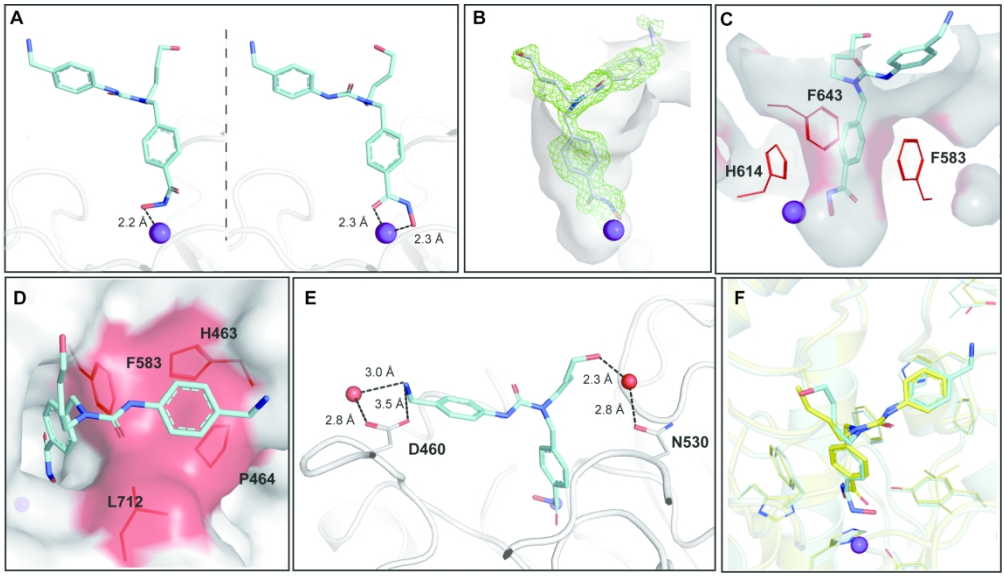
A
2.2 Å
2.3 Å
2.3 Å
B
C
F643
H614
F583
D
H463
F583
P464
L712
E
3.0 Å
3.5 Å
2.8 Å
D460
2.3 Å
2.8 Å
N530
F

Figure 7

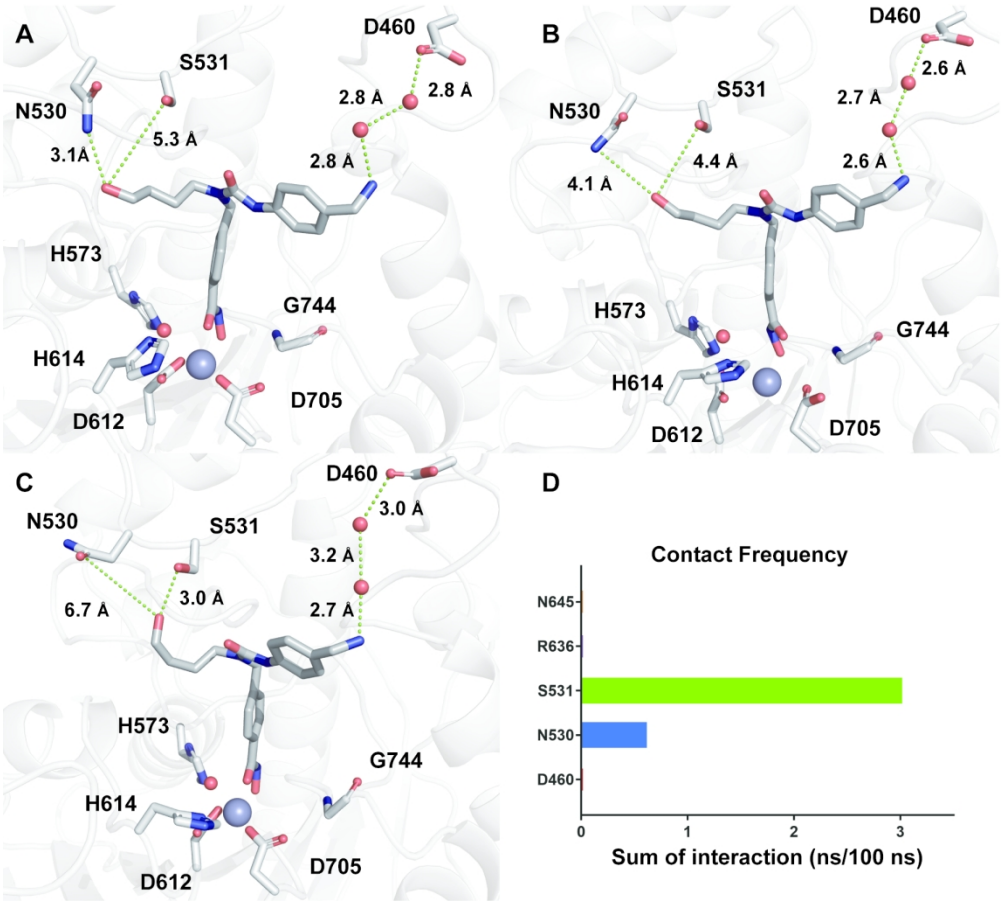
A
D460
S531
N530
2.8 Å
2.8 Å
5.3 Å
3.1Å
2.8 Å
H573
G744
H614
D705
D612
B
D460
2.6 Å
S531
2.7 Å
N530
4.4 Å
2.6 Å
4.1 Å
H573
G744
H614
D705
D612
C
D460
3.0 Å
N530
S531
3.2 Å
6.7 Å
3.0 Å
2.7 Å
H573
G744
H614
D705
D612
D
Contact Frequency
N645
R636
S531
N530
D460
0
1
2
3
Sum of interaction (ns/100 ns)

Figure 8

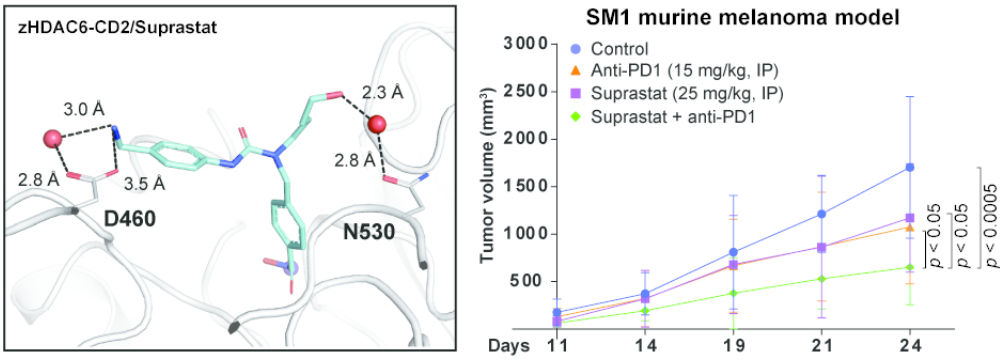
zHDAC6-CD2/Suprastat
3.0 Å
2.8 Å
3.5 Å
D460
2.3 Å
2.8 Å
N530
SM1 murine melanoma model
Control
Anti-PD1 (15 mg/kg, IP)
Suprastat (25 mg/kg, IP)
Suprastat + anti-PD1
Tumor volume (mm³)
3000
2500
2000
1500
1000
500
Days
11
14
19
21
24
p < 0.05
p < 0.05
p < 0.0005

TOC